Noncanonical Activity of Med4 as a Gatekeeper of Metastasis through Epigenetic Control of Integrin Signaling

Authors:
Seong-Yeon Bae[1-4*], Yi Chen[2,5-6], Hong Chen[3,7], Dhiraj Kumar[1-3], Spyros Karaiskos[4], Jane Xu[2,5-6], Chao Lu[2,4], Aaron D. Viny[2, 4-6], Filippo G. Giancotti[1-4†]

Affiliations:

[1]Cancer Metastasis Initiative, Herbert Irving Comprehensive Cancer Center, Columbia University Irving Medical Center, New York, New York 10032, USA
[2]Department of Genetics and Development, Vagelos College of Physicians and Surgeons, Columbia University Irving Medical Center, New York, New York 10032, USA
[3]Department of Cancer Biology, The University of Texas MD Anderson Cancer Center, Houston, Texas 77054, USA
[4]Herbert Irving Comprehensive Cancer Center, Columbia University Irving Medical Center, New York, New York 10032, USA
[5]Columbia Stem Cell Initiative, Vagelos College of Physicians and Surgeons, Columbia University Irving Medical Center, New York, New York 10032, USA
[6]Division of Hematology and Oncology, Department of Medicine, Columbia University Irving Medical Center, New York, New York 10032, USA
[7]Department of Thoracic/Head and Neck Medical Oncology, The University of Texas MD Anderson Cancer Center, Houston, Texas 77054, USA
[†]Deceased

*Correspondence: sb4595@cumc.columbia.edu (S.B.)

Authors' Disclosures

A.D. Viny is in the scientific advisory board for Arima Genomics. All other authors declare no competing interests.

Abstract

Breast cancer metastatic relapse after a latency period, known as metastatic dormancy. Through genetic screening in mice, we identified the mediator complex subunit 4 (*Med4*) as a novel tumor-cell intrinsic gatekeeper in metastatic reactivation. *Med4* downregulation effectively awakened dormant breast cancer cells, prompting macroscopic metastatic outgrowth in the lungs. *Med4* depletion results in profound changes in nuclear size and three-dimensional chromatin architecture from compacted to relaxed states in contrast to the canonical function of the Mediator complex. These changes rewire the expression of extracellular matrix proteins, integrins, and signaling components resulting in integrin-mediated mechano-transduction and activation of YAP and MRTF. The assembly of stress fibers pulls on the nuclear membrane and contributes to reinforcing the overall chromatin modifications by *Med4* depletion. MED4 gene deletions were observed in patients with metastatic breast cancer, and reduced *MED4* expression correlates with worse prognosis, highlighting its significance as a potential biomarker for recurrence.

Significance: This work establishes the first link between Med4 and its role as an epigenetic and transcriptional repressor of ECM programs that reactivates dormant tumor cells in breast cancer metastasis. We highlight the distinct noncanonical role of Med4, in contrast to Med1, as well as the functional implications *in vitro* and *in vivo*. We have functionally validated the aberrant signaling pathways activated through both genetic add back and chemical inhibition and correlate our findings with Med4 expression, metastatic potential, and overall outcome in retrospective patient cohorts.

INTRODUCTION

Survivorship for patients with breast cancer is predicated not by the disease burden in the breast itself, but rather the capability of cells to metastasize outside the breast. Over 90% of patients with breast cancer succumb as a result of distant metastasis. Clinical experience and experimental data in both patients and mouse models show that metastatic disease is the overwhelming cause of breast cancer deaths. Cellular and molecular studies of metastatic breast cancer suggest that disseminating cells from the primary tumor undergo a variable period of dormancy at pre-metastatic sites before undergoing reactivation and outgrowth in macroscopic and life-threatening lesions (1). These data point to a distinct stage of tumor progression whereby organ tropism and quiescence may hallmark both a biomarker of high-risk disease as well as a key therapeutic target. Albeit a small window of opportunity, particularly when the period of clinical latency is short (e.g., TNBC) (2,3) this cellular transformation may represent the keystone to prevention of distant metastasis.

Genomic studies have suggested that macroevolutionary shifts, such as chromosomal instability, contribute to the emergence of cells with metastatic potential from within primary tumors (4). However, their subsequent dissemination and final outgrowth in target organs may be driven by epigenetic mechanisms regulating key features of cellular identity as in epithelial-to-mesenchymal transition (EMT) and stemness/self-renewal (5). Despite their clinical importance, metastatic dormancy and reactivation are poorly understood due to the complexity of the underlying biology. To deconvolve this complexity, we developed a forward genetic screening strategy in the mouse to unveil key regulators of metastatic reactivation (6). Screening of open reading frame (ORF) libraries enabled us to identify several positive regulators of metastatic

reactivation of breast cancer, including Coco, which binds to and inhibits BMP in the lung microenvironment, and the tetraspanin TM4SF1, which mediates non-canonical activation of the JAK2-STAT3 signaling pathway (7,8). In addition, we have found that the master epigenetic regulator PRC1 coordinates stemness and immune suppression at bone metastatic sites in prostate cancer (9).

Collectively, our prior studies suggest that metastatic outgrowth is initiated by a subpopulation of cancer stem cells with metastatic potential (metastasis-initiating cells), which undergo dormancy and reactivation in response to then activation of signaling pathways and transcriptional networks similar to those that govern these processes in adult stem cells (2). However, numerous modulators involved in regulating metastatic dormancy remain to be identified due to the extensive heterogeneity observed in the molecular, genetic, and clinical characteristics of breast cancer metastases. To unveil additional modulators associated with metastatic dormancy, we conducted an *in vivo* CRISPR-Cas9 screen aimed at identifying genetic factors that contribute to breast cancer reactivation in dormant tumor cells. Here we present *mediator complex subunit 4* (*Med4*) as a novel tumor-cell intrinsic gatekeeper in metastatic reactivation.

The Mediator complex regulates Pol II-mediated transcription by adjoining enhancer-bound transcription factors and the general transcription machinery in *cis* (10,11). Mediator, comprising a 26-subunit core organized into head, middle, and tail modules, and a four-subunit dissociable kinase module, manifests functional adaptability due to the variable arrangement of its subunits (12,13). The subunit-specific composition and function of Mediator in its interaction with transcription factors (TF) imply that individual subunits of the complex regulate distinct transcriptional responses (14,15). The molecular basis for the disparate functional roles of individual subunits in various biological contexts remains incompletely understood (16-18), particularly as it pertains to *Med4*. We demonstrated that genetic perturbation of *Med4* awakens dormant tumor cells in pre-metastatic niches. The biological relevance of our findings is supported by the observation that low *MED4* expression is associated with increased risk of metastatic relapse in patients with breast cancer. Taken together, we propose an innovative epigenetic regulatory mechanism whereby *Med4* loss rewires integrin signaling through decompaction of 3-dimensional chromatin architecture.

RESULTS

Med4 enforces dormancy.

To determine novel entities enforcing dormancy, we performed a genome-wide loss-of-function screen using the GeCKO v2 sgRNA library (6,19) (Fig. 1A). Following tail vein injection and lung infiltration, 4T07 cells that had acquired the ability to exit dormancy underwent reactivation and generated macrometastases (Supplementary Fig. S1A). After isolating tumor cells from each metastasis, we cloned and sequenced the integrated sgRNA inserts. Intriguingly, we identified sgRNAs targeting 3 genes (*Med4, Nipbl; Nipped-B-like protein*, and *Esco1; Establishment of sister chromatid cohesion N-acetyltransferase 1*) involved in the formation of super-enhancers (Fig. 1B). Whereas MED4 is a core subunit of the Mediator complex, which connects super-enhancers and promoters in *cis*, NIPBL and ESCO1 aid in loading cohesin onto DNA and hence physically stabilize the assembly of the super-enhancer-promoter complex. We decided to focus on *Med4* because of its inferred biological function, its biological potency *in vivo*, and its potential relevance to human breast cancer. To confirm that *Med4* gene was genuinely edited to

promote metastasis, we performed indel PCR analysis and western blotting in the clone originally isolated from the screen. The results indicated that the clone which contains a sgRNA targeting *Med4*, carried heterozygous instead of homozygous deletion (one allele of the clone carries a nonsense mutation) (Supplementary Fig. S1B-S1E). We hypothesized that *Med4* is an essential gene and examination of the DepMap database supports this hypothesis (Supplementary Fig. S1F) (20). In agreement with the essentiality of *Med4*, we were not able to generate *Med4* KO clones presumably because of strong counterselection. To validate the biological potency of *Med4 in vivo*, we used MirE shRNA targeting *Med4* in 4T07-TGL cells (Supplementary Fig. S1G-S1I) and another syngeneic dormant system, D2A1-d-TGL cells (Fig. 1C-1F). Upon *Med4* silencing, the tumor cells acquired the capacity to efficiently colonize the lung when intravenously injected into immunocompetent mice. To determine if *Med4* silencing specifically induces reactivation from dormancy at the pre-metastatic niche, we used a doxycycline-inducible promoter to express shRNAs targeting *Med4*. Mice were treated with doxycycline either immediately or 2 weeks after tail vein injection (Fig. 1G). Whereas immediate onset of *Med4* knockdown induced metastatic outgrowth at around 2 weeks, a 2-week delay in shRNA expression caused a similar delay in metastatic outgrowth (Fig. 1H-1J), confirming that *Med4* downregulation re-awakens mammary tumor cells from dormancy. Taken together, these findings suggest that *Med4* serves as a sentinel of dormant tumor cells from reactivation.

Lower levels of *MED4* are associated with metastatic relapse in patients.

To examine the potential relevance of our findings to human breast cancer, we first examined the expression of MED4 in multiple metastatic breast cancer datasets from cBioportal (21,22). Analysis of patient datasets indicated that *MED4* has shallow deletions in almost 40% of human breast cancer metastasis samples (Fig. 1K, Supplementary Fig. S2A and S2B) (23). The proportion of breast tumors with deep deletions of *MED4* is extremely low, presumably because *MED4* is an essential gene as aforementioned. Consistently with genomic analysis, paired RNA-seq revealed that mRNA levels of *MED4* are lower but not undetectable in lung, liver, and brain metastases than in matched primary tumors (Fig. 1L) (24). Intriguingly, Kaplan-Meier analysis revealed that *MED4* expression levels could be used to stratify patients into high- and low-risk groups in terms of distant metastasis-free survival; lower MED4 levels were strongly correlated with poor prognosis in patients with advanced breast cancer across subtypes (Fig. 1M, and Supplementary Fig. S2C-S2E) (25). Furthermore, lower levels of *MED4* mRNA could serve as a prognostic indicator for poor overall survival, particularly in subgroups of patients with estrogen receptor-negative (ER-) or human epidermal growth factor 2-positive (HER2+) breast cancer (Supplementary Fig. S2F and S2G). Collectively, these results suggest that MED4's expression level could be a prognostic marker to predict metastatic relapse in breast cancer.

***Med4* loss promotes cancer stem cell traits.**

Phenotypic and functional studies indicated that the *Med4*-silenced cells proliferate modestly slower as compared to control cells under standard culture conditions (Supplementary Fig. S3A and S4A). However, we considered the potential role of *Med4* in regulating the expression of cancer stem cell traits given that the metastasis-initiating cells exhibit functional similarities to cancer stem cells (26). Intriguingly, *Med4*-silenced cells exhibited a substantial increase in their self-renewal capacities, demonstrated by the increased number and size of tumor spheres (Supplementary Fig. S3B and S4B), enhanced clonogenicity (Supplementary Fig. S3C and S4C),

and improved anchorage-independent growth (Supplementary Fig. S3D and S4D). These findings suggest that the silencing of *Med4* induces metastatic outgrowth by augmenting cancer stem cell traits, as observed previously for overexpression of Coco or TM4SF1 (7,8). In addition, *Med4*-deficient cells exhibited increased migratory (Supplementary Fig. S3E and S4E) and invasive (Supplementary Fig. S3F) capacities which are common characteristics of cells undergoing epithelial to mesenchymal transition (EMT) (27). Overall, these results are consistent with the role of *Med4* as a dormancy enforcer and suggest that *Med4* silencing endows dormant tumor cells with self-renewal capacities to produce metastatic outgrowths.

Med4 downregulation reprograms the transcriptional and epigenetic landscape leading to the reinforcement of desmoplastic niche formation, in contrast to the effects of _Med1_.

To obtain a comprehensive view of the transcriptional reprograming in dormancy and metastatic reactivation, we performed bulk RNA sequencing (RNA-seq) of D2A1 (metastatic) cells and its dormant variant D2A1-d cells (28). We identified D2A1_metastatic gene signature (225 differentially upregulated genes in D2A1) and D2A1_dormant gene signature (207 differentially upregulated genes in D2A1-d), respectively (Supplementary Fig. S5A). We employed both signatures in analyzing bulk RNA-seq data from D2A1-d cells expressing two different shRNAs targeting *Med4*, in comparison to a control shRNA. Gene set enrichment analysis (GSEA) indicates that the D2A1_metastatic signature was enriched in *Med4*-silenced cells while the D2A1_dormant signature was enriched in control cells (Supplementary Fig. S5B). This result indicates that *Med4* depletion reprograms transcriptional profile from a dormant to a metastatic state. In addition, RNA-seq revealed that *Med4* silencing skews the transcriptional profile to an active state, antithetical to the canonical function of the Mediator in transcription (14) (Fig. 2A). To determine if the changes in the transcriptional landscape resulting from *Med4* silencing are a general feature of the Mediator complex or specific to *Med4*, we employed MirE shRNA to target the mediator complex subunit 1 (*Med1*) (Supplementary Fig. S5C). MED1 has been the most extensively investigated among the Mediator subunits and is recognized as a prominent transcriptional coactivator and a constituent of super-enhancers (SEs) (10,29). Intriguingly, the silencing of *Med1* resulted in a skewed transcriptional profile towards repression which contrasts with the effect observed with *Med4* silencing (Supplementary Fig. S5D). GSEA using metastatic and dormant signatures also indicated that *Med1* reprograms the transcriptional profile in the opposite direction compared to *Med4* (Supplementary Fig. S5E). Globally the knockdown of either *Med4* or *Med1* did not affect the expression of other mediator complex subunits, suggesting that the observed effects are related to subunit-specific function rather than overall Mediator stoichiometry (Supplementary Fig. S5F-S5H). Thus, we sought to investigate the impact of *Med4* depletion on the three-dimensional (3D) chromatin structure. To map chromatin accessibility comprehensively, we first performed micrococcal nuclease (MNase) digestion assay (30). A titration of MNase revealed that a susceptibility for MNase was elevated in *Med4*-silenced cells especially at the poly-nucleosome part (Fig. 2B). This result suggested that *Med4* silencing decompacts heterochromatic structure in which DNA is tightly packed with nucleosomes. On the contrary, *Med1* silencing resulted in heightened resistance to MNase, suggesting that the downregulation of *Med1* caused chromatin structure to become more compact (Supplementary Fig. S5I). We also confirmed changes in the genome-wide chromatin accessibility landscape by *Med4* silencing using the assay for transposase-accessible chromatin with sequencing (ATAC-seq). The results clearly demonstrated that *Med4* depletion primarily leads to a substantial increase in chromatin accessibility (Fig. 2C). Conversely, *Med1* silencing

had minimal impact on chromatin accessibility (Supplementary Fig. S5J). To delve deeper into the consequences of *Med4* silencing on chromatin structure and transcriptional output, we integrated RNA-seq and ATAC-seq results. Upon depleting *Med4*, the majority of genes exhibited significant changes in chromatin accessibility and gene expression, with increased levels in both accessibility and transcription (Fig. 2D). GSEA revealed that the downregulation of *Med4* induces the expression of signatures reflective of core extracellular matrix proteins (ECMs), assembly of the ECMs, integrin signaling, muscle contraction processes and epithelial to mesenchymal transformation (EMT) (Supplementary Fig. S5K and S5L). Consistent with the results from GSEA, gene ontology (GO) analyses of genes showing concomitant changes in accessibility and gene expression (located in the upper quadrant of the intersection between RNA-seq and ATAC-seq) also indicated significant enrichment of ECM-related and cell-adhesion-related gene signatures (Fig. 2E). In particular, the majority of differentially expressed genes (DEGs) after *Med4* silencing was collagen- (e.g., *Col1a1, Col1a2, Col6a1*), actomyosin-related (e.g., *Acta2, Myl9*), and ECM-remodeling genes (e.g., *Loxl3, Mmp2, Adamts5*) (Fig. 2F). This suggests that *Med4* depletion is associated with stiffening matrices surrounding cancer cells, so called desmoplasia, which is a critical manifestation of cancer progression (31-33). Consistently, immunohistochemistry (IHC) of α-SMA (a protein coded by *Acta2*) and Masson's trichrome stain, which labels collagen, validated the substantial desmoplastic stromal reaction in metastases induced by *Med4* silencing compared to the dormant niche (Fig. 2G). Collectively, these results indicate that *Med4* deficiency bolsters matrix stiffening, which creates a favorable environment conducive to the metastatic outgrowth.

Med4 silencing alters nuclear architecture and decompacts 3D chromatin organization by increasing cytoskeletal tensile forces.

Although a growing body of evidence indicates that Mediator exerts on enhancer-promoter looping functionally rather than structurally, Mediator has been implicated in super-enhancer formation and promoter-enhancer looping orchestrating with the cohesin ring (11,34). It is thereby conceivable that Mediator plays a role in both maintaining and modifying chromatin architecture. Thus, we sought to visualize the chromatin structure by staining HP1α, a component of constitutive heterochromatin (35). Intriguingly, *Med4*-deficient cells displayed a sparse distribution of heterochromatin foci accompanied by an increase in nuclear size, whereas the control cells exhibited a condensed heterochromatin structure (Fig. 3A, and Supplementary Movies 1-3). In contrast, *Med1*-deficient cells did not exhibit significant changes in the distribution of heterochromatin foci (Supplementary Fig. S6A, and Supplementary Movies 4-6). These findings indicate that *Med4* plays a role in controlling chromatin and nuclear architectures. Given that the nuclear lamina is known to anchor the heterochromatin structure to the nuclear periphery and be associated with gene silencing, we hypothesized that the nuclear lamina plays a crucial role in the alterations of heterochromatin structure caused by *Med4* silencing (36,37). To investigate this, we co-stained the cells with LAMIN A/C and H3K9me3, another marker for heterochromatin. Interestingly, we observed that H3K9me3 was dislodged from the nuclear lamina in *Med4*-depleted cells, whereas it remained colocalized in control cells (Fig. 3B). Overall, these findings indicate that the depletion of *Med4* leads to the decompaction of the 3-dimensional chromatin structure. Furthermore, in *Med4*-depleted cells, we observed a reduction in the densities of LAMIN A/C at the nuclear periphery, accompanied by an enlargement in nuclear size (Fig. 3C and 3D). Notably, the overexpression of *MED4* had the ability to reverse nuclear enlargement and restore the distorted nuclear lamina. However, such changes were not

observed in *Med1*-deficient cells (Supplementary Fig. S6B). These results led us to hypothesize that *Med4* could potentially alter the solubility of LAMIN A/C. To investigate this, we detected p-LAMIN A/C (Ser^{22}) (38,39) and total LAMIN A/C, followed by sub-fractionating the nucleoplasm and nuclear envelope (Supplementary Fig. S6C). However, our results did not reveal any changes in LAMIN solubility caused by *Med4* silencing. Since the stress fibers are connected to the matrix via integrins and to the nuclear membrane through the LINC complex (40), heightened tension in the actin cytoskeleton could conceivably increase the size of the nucleus by exerting radial forces on the nuclear membrane. To investigate the impact of cytoskeletal tensile forces on the alterations in nuclear size and architecture resulting from *Med4* depletion, we used actin polymerization inhibitors, cytochalasin D, or latrunculin B (41). Remarkably, upon treating the cells with these actin cytoskeleton disruptors, we observed a reversal of the changes in nuclear size and architecture caused by *Med4* silencing (Fig. 3E). Furthermore, disrupting the actin cytoskeleton resulted in the reversal of the dispersed heterochromatin structure observed in *Med4*-deficient cells (Fig. 3F and Supplementary Fig. S6D). These results suggest the reduction of MED4 leads to elevated expression of ECM proteins and the assembly of stress fibers. These stress fibers apply tension to the nuclear membrane, potentially facilitating or reinforcing alterations in chromatin structure.

Med4 deficiency promotes cell growth within a desmoplastic niche by activating integrin signaling.

Considering the increasing body of evidence supporting the impact of biochemical and biomechanical cues derived from the extracellular matrix (ECM) on cancer cell metastatic abilities, we sought to examine if *Med4* mediates outgrowth in response to the stiffness and composition of matrices. To model the normal ductal microenvironment characterized by a basement membrane-rich ECM, and the stiff tumor microenvironment enriched in collagen I (32,42), we placed control and *Med4*-silenced breast cancer cells in two different conditions: (1) 3D Matrigel, representing the basement membrane-rich ECM, and (2) 3D Matrigel plus collagen I, which recapitulates the tumor microenvironment. Strikingly, *Med4* silencing promoted tumor organoid growth and invasion in stiff 3D matrices (Matrigel + collagen I), while cells maintained a spherical growth pattern in the soft 3D matrices (Matrigel-only) regardless of their *Med4* expression (Fig. 4A). Ki67 staining indicated that *Med4* inactivation increases cell cycle progression in stiff 3D matrices but slightly decreases it in 2D culture (Fig. 4B). These data indicate that cells in a *Med4*-deficient background can preferentially grow in the desmoplastic niche. Collectively, these results indicate that *Med4* deficiency not only induces matrix stiffening, fostering a favorable environment for metastatic outgrowth, but also stimulates the tumor-cell intrinsic survival and proliferative abilities within the established metastatic niche.

To exit dormancy, metastatic tumor cells are required to extend lamellipodia and establish productive interactions with the matrix. Adhesion molecules, particularly integrins, play a crucial role in transmitting external stimuli from the ECM (43). These integrins are integrated into focal adhesion (FA) complexes, which connect the cytoskeleton to the ECM, enabling the reciprocal transmission of forces between cells and the surrounding microenvironment (44). Given the pivotal role of integrins in cell adhesion and signaling, along with the transcriptional alterations in the ECM composition (Fig. 2E) and integrin repertoire (Supplementary Fig. S7A) by *Med4* silencing, we hypothesized that *Med4* deficiency promotes metastatic reactivation by activating integrin-mediated signaling. Immunofluorescence analysis revealed that *Med4*-silenced cells exhibit a more organized actin cytoskeleton and more numerous focal adhesions containing

activated FAK (p-FAK Y^{397}), paxillin, and vinculin (Fig. 4C). Also, $p130^{Cas}$, JNK, p38, AKT, and MLC2 phosphorylation were significantly increased upon *Med4* depletion (Fig. 4D). Furthermore, we validated that *Med4*-deficient cells exhibited increased formation of aligned stress fibers and focal adhesions in a Matrigel + collagen I environment, indicating that the downregulation of *Med4* enhanced integrin-mediated adhesion in the 3D culture setting (Fig. 4E). In order to corroborate the implication of integrin signaling activation in the growth of organoids due to *Med4* silencing, we employed defactinib, a targeted inhibitor of FAK (45). Remarkably, the application of defactinib demonstrated a marked reduction in the invasive proliferation of *Med4*-deficient cells within the 3D Matrigel + collagen I matrix (Fig. 4F). Collectively, these findings provide evidence indicating that *Med4* silencing triggers the activation of integrin signaling.

Med4 loss promotes metastatic reactivation by activating integrin-mediated nuclear mechanosensing.

To identify the top transcription factors controlling the transcriptome changes by *Med4* silencing, we applied ChIP-X Enrichment Analysis 3 (ChEA3) transcription factor enrichment analysis to the RNA-seq data (46). Notably, we found that SRF, and TEAD 1/2 cistromes govern the transcriptional reprogram by *Med4* depletion along with EMT cistromes (Fig. 5A). Also, *de novo* motif enrichment analysis performed on genes exhibiting concurrent increases in accessibility and gene expression following *Med4* silencing confirmed the enrichment of TEAD, TEAD4, and SRF motifs (Fig. 5B). SRF, a co-factor for myocardin-related transcription factor (MRTF), and TEADs, transcriptional co-activators for YAP and TAZ, are major mechanosensitive transcriptional factors that transduce mechanical cues by the cytoskeleton to gene expression in response to integrin-mediated adhesion. GSEA results revealed that the gene signatures for MRTF/SRF (47) and for YAP (48) are enriched in *Med4*-deficient cells (Fig. 5C). In response to both biochemical and mechanical signals, YAP undergoes translocation from the cytoplasm to the nucleus, where it interacts with and triggers the activation of the TEAD transcription factor (49). MRTF binds stoichiometrically to soluble G-actin and is released as a consequence of actin polymerization and formation of stress fibers. Once released from G-actin, MRTF enters into the nucleus, where it functions as a co-factor for SRF, which drives expression of cytoskeletal genes in a feed forward loop (50). Hence, we sought to examine the cellular localization of these transcription factors. Immunofluorescence results revealed that *Med4* silencing led to the predominant nuclear localization of both MRTF-A and YAP (Fig. 5D). Consistent with these results, expression of MRTF/SRF target genes(51,52), YAP/TEAD target genes (53), and shared MRTF and YAP target genes were activated in *Med4*-deficient cells, confirming these mechanosensitive transcription factors were activated by Med4 depletion (Supplementary Fig. S7B). Restoring MED4 expression by overexpressing MED4 cDNA led to the relocation of MRTF-A to the cytoplasm and resulted in the reversal of the activation of MRTF-A/SRF target gene expression (Fig. 5E, 5F and Supplementary Fig. S7C). Immunohistochemistry of lung sections unveiled that a notable portion of macrometastases originating from *Med4*-deficient cells exhibited positive staining for nuclear MRTF-A and YAP, in contrast to micrometastases originating from control cells which exhibited negative nuclear staining of these factors (Supplementary Fig. S7D). To determine if these integrin-mediated mechanosensitive transcription factors play a pivotal role for *in vivo* metastatic reactivation by *Med4* loss, we ablated these mechanosensitive transcription factors though shRNA silencing and injected into immunocompetent BALB/c recipients (Supplementary Fig. S7E). Silencing *Mrtfa*, *Srf*, or *Yap* +

Taz abrogated the metastatic capacity of *Med4*-silenced cells, pointing to a requirement for these transcriptional regulators in the process of metastatic reactivation (Fig. 5G). These findings indicate that the depletion of MED4 triggers metastatic reactivation through the initiation of integrin-driven mechano-transduction, consequently leading to the activation of MRTF-SRF and YAP/TAZ signaling pathways.

DISCUSSION

The Mediator complex is implicated in multiple molecular functions encompassing epigenetic regulation, transcriptional elongation, termination, mRNA processing, noncoding RNA activation and super-enhancer formation(54); yet the exact mechanisms through which this plastic and multimeric complex coordinates multiple transcription factors remain unclear. In addition, whereas MED1 is likely involved in the formation of super-enhancers and transcriptional activation, which drive the expression of key cell-identity genes (10,29) as well as oncogenic transcription factors (55-57), both the physiological and pathophysiological roles of MED4 is poorly understood. Interestingly, in public datasets from large scale transcriptional profiling efforts, down-regulation of *MED4* has been correlated with cervical cancer and retinoblastoma (58-60) . This study represents the first description of MED4 as a non-canonical Mediator component and transcriptional repressor and the first description of MED4 being implicated in metastasis, highlighting its potential role as a gatekeeper for metastatic relapse. Intriguingly, the epigenetic and transcriptional reprogramming effects observed by *Med4* silencing were in stark contrast to the canonical function of the Mediator complex and specifically of *Med1*. This component-specific disparity identifies a unique and directionally oppositional function that MED4 serves within the context of Mediator-mediated transcription. These findings highlight tissue-specific and gene-specific epigenetic mechanisms of control, hereby in this setting, resulting in aberrant ECM remodeling, integrin-mediated mechano-transduction, and facilitating the emergence of tumor cells from dormancy within metastatic niches. Our results demonstrate that MED4 inactivation contributes to the stiffening of the extracellular matrix (ECM) and the activation of integrin-mediated mechano-transduction. This is in concert with the euchromatinization and activation of MRTF/SRF and YAP/TAZ transcription factor programs. Taken together, we posit that *Med4* loss results in decompaction of the three-dimensional chromatin structure, hereby unlocking ECM gene expression programs. We show that this epigenetic and transcriptional activation facilitates a functional and permissive cellular tropism both *in vitro* and *in vivo*.

We demonstrate that *Med4* deficiency has the potential to initiate metastatic reactivation within the context of breast cancer. Interestingly, our analysis reveals that *Med4* silencing predominantly stimulates a transcriptional profile consisting of ECM-related genes, which stands in contrast to the Mediator's conventional role in transcription. Conversely, the silencing of *Med1* displayed a distinct pattern of transcriptome regulation, highlighting the considerable flexibility of the complex contingent on its subunit composition. Sun and colleagues conducted a shRNA screening targeting individual subunits of transcription factor IID (TFIID) and the Mediator complex (34). Disrupting various subunits yielded distinct effects on the transcriptome of mouse embryonic stem cells (mESCs), even within subunits of the same complex. Their shRNA-based screen, similar to our findings, revealed that *Med4* shRNA altered transcriptome towards activation, and gene ontology analysis of the up-regulated gene list highlighted the enrichment of ECM signatures. However, when they employed the auxin degron system for the acute

degradation of MED4, it minimally affected the integrity of the Mediator complex and resulted in transcriptome downregulation by decreasing RNA polymerase II recruitment to the promoters. Hence, it is plausible that a dosage effect whereby *Med4* knockdown as opposed to complete knockout drives the pathological phenotype.

The spatial arrangement of chromosomes within the nucleus represents an important layer of transcriptional regulation. Recent research has shown that heterochromatin is connected to the nuclear lamina, and mechanical forces are conveyed to interactions between the lamina and chromatin(61,62). The nucleus has been proposed as a mechanosensor that detects biochemical and mechanical signals from cellular adhesions through the actin cytoskeleton (63). This interaction directly leads to the stretching of chromatin, resulting in enhanced transcription (64). Our data revealed that *Med4*-depleted cells exhibited larger nucleus and decondensed chromatin structure (Fig. 3A). Given that stress fibers link the matrix through integrins and the nuclear membrane via the linker of nucleoskeleton and cytoskeleton (LINC) complex (40), increased tension within the actin cytoskeleton could potentially enlarge the nucleus by applying radial forces to the nuclear membrane. These enlarged nuclei could potentially lead to the relaxation of the three-dimensional chromatin structure and increase expression of genes encoding ECM and cytoskeletal components. The mechanism by which the force-induced activation is selectively applied to particular genes remains elusive. One possibility is transcriptional feedback of MRTF/SRF on mechanoadaptation (52,65,66). Upon cytosolic F-actin polymerization, the MRTF/SRF system is activated and stimulates the expression of genes associated with extracellular matrix (ECM), adhesion, and the cytoskeleton. Thus, it is conceivable that this mechanoadaptation through mechanosensitive transcription factors contributes to the reinforcement of the phenotype resulting from Med4 silencing. In order to articulate this feed-forward loop between cytoskeletal tensile forces and ECM gene expression by *Med4* silencing, a comprehensive analysis of the transcriptome and epigenetics after disrupting the LINC complex by introducing a dominant-negative KASH (DN-KASH) could provide further insights.

We noted that cells with reduced *Med4* levels exhibit decreased fitness when cultured in a 2D environment (Supplementary Fig. S3A and S4A). However, under conditions involving 3D Matrigel + collagen I or tumorsphere growth, the *Med4*-silenced cells displayed notable enhancement in growth and the formation of spheres (Fig. 4A and 4B). In addition, *Med4*-deficient cells showed higher proliferative capacity and ECM and collagen deposition levels in the lung parenchyma (Fig. 2G). These findings suggest that a *Med4*-deficient tumor cell not only leads to create a desmoplastic niche that supports the growth of metastatic cells but also stimulates the intrinsic survival and proliferative capabilities of tumor cells within the established metastatic microenvironment. However, the precise mechanism behind this heightened adaptability in a 3D culture context has yet to be elucidated. A recent study about *MED12 Gly-44* mutations in the context of leiomyoma revealed findings in line with our results (67). While *MED12 Gly-44* mutant cells displayed a proliferation deficiency under 2D culture conditions, these mutants formed notably larger spheroids in 3D spheroid environments compared to wild-type cells. The *MED12* mutations led to changes in the transcriptome, resulting in the expression of collagen and ECM genes, and these transcriptomic alterations were further magnified in 3D conditions. Thus, it is plausible that the Mediator might play a pivotal role in modulating cellular adaptability within the tumor microenvironment through ECM remodeling though the precise molecular pathways triggered by *Med4* deficiency, which contribute to this increased adaptability, are yet to be precisely identified. Among potential mechanisms, one notable avenue

is that *Med4* potentially alters the integrin repertoire, leading to an augmentation in the expression of collagen receptors such as integrin α2β1 (Supplementary Fig. S7A). Further insights could be gained through additional transcriptome and epigenetic analyses conducted under varying culture conditions.

Current adjuvant breast cancer therapeutic regimens are aimed to prevention of metastatic relapse, and despite the prognostic value of pathological, genomic, and transcriptional testing, late metastasis occurs in nearly 25% of patients (68). Elucidating the molecular mechanisms that enable dormant tumor cells to evade the immune system and survive under stress at pre-metastatic sites, as well as identifying subsets of patients who could benefit from therapy targeting these mechanisms, would greatly reduce the mortality related to metastatic relapse. We found that a large fraction of metastatic breast cancer samples from patients have shallow *MED4* deletions (Fig. 1K, Supplementary Fig. S2A and S2B), and lower *MED4* levels correlated with poor prognosis in patients with advanced breast cancer across subtypes (Fig. 1M and Supplementary Fig. S2C), indicating that MED4 likely has a substantial role in governing metastasis in breast cancer patients.

Our findings highlight the potential and mechanistic basis for *MED4* expression and related gene signatures as a biomarker of metastatic dormancy. Future studies will be aimed to determine if *MED4* expression may be able to stratify patients prone to recurrence, enabling the identification of subsets at high risk for subclinical metastasis and may uniquely benefit from therapeutic intensification. Moreover, these data lay the foundational groundwork for novel strategies targeting effectors activated by MED4 loss including early phase inhibitors of the FAK or YAP/TEAD pathways.

METHODS

Animal studies

Mouse studies were conducted in accordance with protocols approved by the Institutional Animal Care and Use Committee of Columbia University and MD Anderson Cancer Center. Six-week-old female mice BALB/c were purchased from The Jackson Laboratory.
To examine lung colonization, 4T07 (3.0 x 10^5), D2A1-d (2.0 x 10^5), and D2A1 (2.0 x 10^5) mammary carcinoma cells were resuspended in 100 µl of PBS and injected into the lateral tail vein.
Doxycycline (Dox) was administered to mice through water *ad libitum* (2 mg/ml). For inducible shRNA experiments, Dox was administered either immediately after injection (Dox day 0) of the cancer cells or 14 days later (Dox day 14). Bioluminescence (BLI) was used to examine metastatic outgrowth. Metastatic lesions were confirmed by postmortem dissection.
For bioluminescent imaging, mice were anesthetized and injected retro-orbitally with 1.5 mg (75 mg/kg) of D-luciferin (Gold Biotechnology; LUCK-1G) at the indicated times after injecting cells. Animals were imaged in an IVIS Spectrum chamber within 5 min after D-luciferin injection, and data were recorded using Living Image software (PerkinElmer). To measure lung colonization, photon flux was calculated for each mouse by using a circular region of interest encompassing the thorax of the mouse. After subtracting a background value obtained from a control mouse injected only with D-luciferin, photon flux was normalized to the value obtained 30 min after injection of the tumor cells. This latter value was arbitrarily set at 100.

Cell lines

The 4T07 cell line was generously provided by Dr. Fred Miller (Wayne State University, Detroit, MI) and cultured as described (69). The D2A1-d and D2A1 cell lines were generously provided by Dr. Robert Weinberg (MIT, Boston, MA) and cultured as described(28). HEK293FT cells (from Thermo Fisher Scientific) was cultured per the manufacturer's protocol. For bioluminescent tracking, cell lines were infected with a lentiviral vector encoding herpes simplex 3 virus thymidine kinase 1, green fluorescent protein (GFP) and firefly luciferase. GFP-positive cells were isolated by FACS.

Genome-wide CRISPR-Cas9 screening.

A forward genetic screening was performed as described in with a minor modification (6). The GeCKO v2 library A was obtained from Addgene (1000000052) and was amplified and packaged in lentiviruses as described previously(19). The viral titer was determined by limiting dilution-colony counting. 4T07 cells were transduced with the library at the MOI of 0.3 to ensure one sgRNA/cell. Library-transduced cells were selected with 2 µg/ml of puromycin for 7 days, and then injected through tail vein of 6-week-old female BALB/c mice. Mice were monitored weekly by bioluminescent imaging and lung metastases were confirmed by postmortem dissection at 3-4 weeks after injecting library-transduced cells. Macroscopic lung nodules were dissected separately and digested in Collagenase Type IV (Stem Cell technologies; 07909) at 37°C for 1.5 h with rocking. After centrifuging at 1,000 rpm for 3 min, pellets were resuspended in the complete medium and filtered through 35 µm strainers. Isolated clonogenic tumor cells were expanded in 4 µg/ml of puromycin medium. Genomic DNAs were isolated using Maxwell®

RSC Cultured Cells DNA Kit (Promega; AS1620) according to the manufacturer's protocol. Inserted sgRNA sequences were amplified by PCR with the following primers and thermocycling parameters (v2Adaptor-F: 5'-AATGGACTATCATATGCTTACCGTAACTTGAAAGTATTTCG-3', v2Adaptor-R: 5'-TCTACTATTCTTTCCCCTGCACTGTTGTGGGCGATGTGCGCTCTG-3'; 95°C for 2 min, 30 cycles of (98°C for 1 s, 60°C for 5 s, 72°C for 35 s), and 72°C for 1 min)
All PCR was performed using KAPA HiFi HotStart ReadyMix (Kapa Biosystems; KK2602). The PCR products were isolated by QIAquick PCR Purification Kit (Qiagen; 28104) and subjected to Sanger sequencing. To validate hits, the sgRNAs were cloned in lentiCRISPR v2 vector, and transduced into 4T07-TGL cells. Transduced clones were injected through tail vein of 6-week-old female BALB/c mice and lung metastases were monitored weekly by bioluminescent imaging.

Indel analysis for validating a knockout screening.

A pair of primers was designed to amplify the 250-300 bp region centered around the sgRNA cut site (GRCm39 chr.14 73752726-73752745). 300 ng of genomic DNA isolated in *Genome-wide CRISPR-Cas9 screening* was amplified by PCR with the following primers and thermocycling parameters (*Med4* indel primer_F: 5'-CACGGCCATGGCTTTCTAAC-3', *Med4* indel primer_R: 5'- GAGGGTTGTGAGCTACGTGT-3'; 95°C for 2 min, 30 cycles of (98°C for 1 s, 60°C for 5 s, 72°C for 35 s), and 72°C for 1 min). PCR was performed using NEBNext® High-Fidelity 2X PCR Master Mix (NEB; M0541S). The purified PCR products were separated by a 4-20% TBE gel (Invitrogen; EC62252BOX) and stained with GelRed for 1 hr. The bands were visualized by ChemiDoc (Bio-Rad).

DNA constructs for overexpression and silencing.

The cDNA encoding human *MED4* was obtained from Addgene (15425). The cDNA was sub-cloned in FLAG-HA-pcDNA3.1- (Addgene; 52535) to generate N-terminally Flag-HA tagged MED4 cDNA. The N-term Flag-HA-MED4 cDNA was sub-cloned in pCDH-EF1-MCS-IRES-Neo (System Biosciences; CD502A-1) and verified by sequencing. The shRNAs were designed using the SplashRNA algorithm(70). shRNA sequences are shown in Supplementary Table S1.

Cell growth assay

Cells were seeded at a density of 1.0 x 10^5 cells onto 6 cm dishes (D2A1-d cells) or 10 cm dishes (4T07 cells) at Day 0. Cells were trypsinized and counted at the indicated.

Tumorsphere assay

Single cells suspension of 4T07, D2A1-d, and D2A1 cells (10,000 cells/ 2 ml) were plated on 6-well ultra-low attachment plates for tumorsphere cultures. Cells were cultured in serum free MEBM supplemented with 1:50 B27, 10 ng/ml bFGF (BD Biosciences;) and 20 ng/ml EGF (BD Biosciences;) and 4 ug/ml insulin, 4 ug/ml heparin, and 0.4% BSA for 10 days. Tumorsphere were visualized under phase contrast microscope, photographed and counted by GelCounter and represented graphically.

Soft agar colony formation assay

6-well culture plates were coated with 1 ml of 0.6 % Low Melt Agarose (Bio-Rad; 1613111). Cells were diluted at a density of 1.0 x 10^4 cells/ml in media containing 0.3% Low Melt Agarose and seeded 1 ml/ well. After 10 days, cells were stained with 0.005% crystal violet in 10% neutral buffered formalin (NBF) for 30 min at R.T. Soft agar was destained with distilled water until the background got clear. Colonies were scanned for visualization and counted manually.

3D culture

8-well chamber slides were coated with either 100 µl of 100% Matrigel (Corning; 354263) or 50% Matrigel + 50% Collagen I (Corning; 354236) at 37°C for 30 min prior to cell seeding (71). Cells were seeded onto the matrix at a density of 400 cells/100 µl/well.

Clonogenicity assay

For measuring clonogenicity capacities, D2A1-d and 4T07 cells were seeded onto 10 cm dishes at a density of 1,000 cells. After 6 days, the morphology and size of colonies were captured by a phase-contrast microscopy. Cells were fixed with 100% methanol for 20 min and stained with 0.5% crystal violet in 20% methanol for 5 min. Then plates were destained with PBS until the background got clear. The images of whole plates were taken by a scanner and colonies were counted manually.

Transwell migration/invasion assay

Migration assays were performed as previously described in (72) with minor modification. using uncoated cell culture inserts with 8 µm pores (Corning; 3422) according to manufacturer's instructions. Briefly, D2A1-d and 4T07 cells were harvested with Trypsin/EDTA and resuspended in serum-free medium at a density of 1.0 x 10^5 cells/ml for D2A1-d and 2.0 x 10^5 cells/ml for 4T07. 100 µl of cells were seeded into the upper chamber of uncoated cell culture inserts with 8 µm pores (Corning; 3422). Lower chambers were filled with 650 µl medium containing 10% FBS as a chemoattractant. After 18 hours, cells were fixed and permeabilized with 70% ethanol for 15 min and stained with 0.1% crystal violet/10% ethanol for 20 min. The non-migrating cells on the upper surface of the filter were removed by cotton swab. The number of migratory cells was measured by counting at × 200 magnifications using a microscope. For invasion assays, Matrigel was diluted in ice-cold serum-free medium to a concentration of 300 µg/ml. 100 µl of diluted Matrigel solution was added into the upper chamber and incubated at 37°C for 30 min to coat the membrane. D2A1-d (1.0 x 10^4 cells) and 4T07 (3.0 x 10^4 cells) cells were seeded into the upper chamber and incubated for 24 hours. The following procedure was performed as described above.

Micrococcal nuclease digestion assay (MNase digestion assay)

Global chromatin accessibility was assessed by MNase digestion assay as described previously (73) with minor modification. 1 million cells were cross-linked with 1% formaldehyde for 10 min at R. T. and quenched with 125 mM glycine for 5 min. Cells were washed once with cold PBS and collected by centrifuging at 1,000 rpm for 5 min at 4°C. Fixed cells were re-suspended

in lysis buffer (10 mM Tris-HCl, pH7.5, 10 mM NaCl, 0.5% NP-40) and incubated on ice for 10 min. After centrifugation, the cell pellets ware washed once with MNase digestion buffer (20 mM Tris-HCl, pH7.5, 15 mM NaCl, 60 mM KCl, 1 mM $CaCl_2$). After re-suspended in 250 µl MNase digestion buffer with proteinase inhibitors, 62.5 units per 1 million cells MNase (NEB; M0247S) was added to resuspended pellets. After incubation at 37°C for the indicated time, 250 µl of STOP buffer (100 mM Tris-HCl, pH 8.1, 20 mM EDTA, 200 mM NaCl, 2% Triton X-100, 0.2% sodium deoxycholate) was added. Lysates were sonicated for 4 cycles (30 sec on and 30 sec off) in Bioruptor and supernatant was collected after centrifugation. The supernatant was reverse-crosslinked at 65°C overnight and treated with RNase A at 37°C for 1 h and Proteinase K at 55°C for 2 h. The DNA fragments were purified by ethanol precipitation and analyzed by agarose gel electrophoresis.

Immunofluorescence

For staining cells on 2D culture, cells were rinsed with PBS once and fixed with 4% paraformaldehyde (PFA) in PBS for 15 min. Cells were washed three times with PBS for 5 min followed by permeabilizing with 0.5% Triton X-100/PBS for 5 min. After rinsing once with PBS, cells were blocked with 1% BSA/0.3% Triton X-100/PBS for 1 h. Next, cells were incubated in primary antibodies diluted in the blocking buffer at 4°C overnight followed by incubating in the secondary antibodies for 1 h R.T. After washing once with PBS, nuclei were counter-stained with DAPI (1:1000 in PBS) for 5 min followed by mounting.
For staining cells on 3D culture, cells were fixed with 2% PFA in PBS supplemented with 50 mM glycine for 30 min at R.T. After washing three times for 20 min with PBS supplemented with 50 mM glycine, cells were blocked with 10% normal goat serum in the IF buffer (0.1% BSA, 0.2% Triton X-100, 0.05% Tween-20 in PBS) at R.T. for 1 h. Primary antibodies were diluted in the blocking buffer and subjected to cells. After overnight incubation at 4°C, cells were washed with the IF buffer for 20 min three times and followed by incubating with secondary antibodies (diluted in the blocking buffer) for 1 h at R.T. After washing once with the IF buffer, nuclei were counter stained with DAPI for 5 min, followed by mounting.

Immunohistochemistry

Immunostaining of mouse lungs was performed as previously described (8). In brief, tissues were fixed in 10% neutral buffered formalin for 24 hours, embedded in paraffin, sectioned, and stained with hematoxylin and eosin (H&E) for histopathological evaluation. For immunohistochemistry, unstained slides of sectioned tissues were deparaffinized and epitope/antigen retrieval was performed with 10 mM sodium citrate (pH 6.0). The slides were treated with 3% H2O2 to block endogenous peroxidase. The slides were then incubated in 5% normal goat serum/5% BSA/0.3% Triton X-100/PBS and stained with the appropriate primary antibodies. After an overnight incubation in primary antibodies, slides were stained with secondary antibodies and DAPI before mounting with the Vectashield mounting medium (Vector Laboratories).

Western blot

Protein lysates were harvested with RIPA lysis buffer (Sigma Aldrich; R0278) containing protease inhibitor cocktail (Thermo Fisher Scientific; 78429), phosphatase inhibitor 2 and 3

(Sigma Aldrich; P5726and P0044). Samples were standardized for protein concentration using the Pierce BCA protein assay (VWR 23227), and incubated at 100 °C for 10 min under reducing conditions. After denaturation, samples were separated by Bolt 4–12% Bis-Tris Plus Gels (Thermo Fisher Scientific NW04125BOX) and transferred onto a PVDF membrane using iBlot Transfer Stacks (Thermo Fisher Scientific IB401001). Blots were blocked with 5% bovine serum albumin (BSA) in TBST for 1 h at room temperature. Blots were then probed with different primary antibodies (listed in Supplementary Table S2) in the blocking buffer overnight at 4 °C. Blots were washed with TBST for 10 min three times before incubation with secondary antibodies [Anti-rabbit IgG-HRP (Cell Signaling Technology 7074S, 1:5000), Anti-mouse IgG-HRP (Cell Signaling Technology 7076S, 1:5000), anti-goat IgG-HRP (Santa Cruz Biotechnology sc-2354, 1:5000)] in 2.5% BLOT-QuickBlocker (G Biosciences 786-011) in TBST for 1 h at room temperature. Blots were washed with TBST and imaged using chemiluminescent substrate [Pierce ECL (Thermo Fisher Scientific 32209), SuperSignal West Pico PLUS (Thermo Fisher Scientific 34577), or SuperSignal West Femto (Thermo Fisher Scientific 34096)] on the ChemiDox XRS + (Bio-Rad).

Real time PCR analysis

Total RNA was extracted using the Maxwell® RSC simplyRNA Cells and RNase-free DNase Kit (Promega; AS1390) using an automated RNA/DNA isolation instrument (Maxwell, Promega). cDNAs were synthesized using High-Capacity cDNA Reverse Transcription Kit (Applied Biosystems; 4368814). cDNA corresponding to approximately 10 ng of starting RNA was used for one reaction. qRT-PCR was performed with PowerUp SYBR Green Master Mix (Applied Biosystems) on QuantStudio™ 7 Flex Real-Time PCR System. All quantifications were normalized to endogenous GAPDH. Primer sequences used to amplify genes were purchased from Sigma-Aldrich and are listed in Supplementary Table S3.

Bulk RNA-sequencing and analysis

Total RNA was isolated as described above. RNA-sequencing was performed by the BGI sequencing facility in Hong Kong. RNA quality, including RNA concentration, RIN value, 28S/18S ratio, and fragment length distribution was confirmed with an Agilent 2100 Bio analyzer (Agilent RNA 6000 Nano Kit). Libraries were prepared by using the standard methodology and run on a BGISEQ-500 platform. Raw reads were quality-checked and subsequently mapped to the mouse genome (mm10_UCSC) through the Spliced Transcripts Alignment to a Reference (STAR)(74), which outputs a BAM file containing both the sequence and its genomic coordinate. Together with a General Transfer Format (GTF) the file containing all the genomic annotations were used to determine the total number of reads per transcript using the HTSeq Count program.(75) Differential gene expression was analyzed by using the DESeq2 algorithm(76) with $|\text{fold change}| \geq 2$ and FDR < 0.05. Gene set enrichment analysis (GSEA) was performed on a pre-ranked gene list that was generated based on the gene expression changes between shMed4 and control cells(77). Gene expression data were transformed in logarithmic scale and normalized accordingly. Heatmaps showing the gene expression differences between control and Med4 KD cells were generated by using the Morpheus online tool (https://software.broadinstitute.org/morpheus/).

ATAC-sequencing and analysis

Chromatin accessibility assays utilizing the bacterial Tn5 transposase were performed as described with minor modifications (78). Cells (5.0 x 10^4) were lysed and incubated with transposition reaction mix for 30 minutes at 37°C. Samples were PCR-amplified and sequenced on an Illumina NextSeq 500.

Bulk ATAC-seq raw data were pre-processed using the nfcore/atacseq pipeline version 2.0 (10.5281/zenodo.2634132), implemented in Nextflow (version 22.10.2). Reads were trimmed for both quality and Illumina adapter sequences using 'trim_galore' then aligned to mouse assembly mm10 with BWA using the default parameters. Aligned reads with the same start site and orientation were removed using the Picard tool MarkDuplicates (http://broadinstitute.github.io/picard). Density profiles were created by extending each read to the average library fragment size and then computing density using the BEDTools suite (http://bedtools.readthedocs.io). Reads were not extended when generating ATAC-seq read density. Enriched regions were discovered using MACS2 and scored against matched input libraries (|fold change| > 2 and p-value < 0.005). Peaks were then filtered against genomic 'blacklisted' regions and filtered peaks within 500 bp were merged to create a full peak atlas. Raw read counts were tabulated over this peak atlas using featureCounts (http://subread.sourceforge.net). All genome browser tracks and read density tables were normalized to a sequencing depth of ten million mapped reads. Peaks were annotated using linear genomic distance, with a gene assigned to a peak if it was within 50 kb upstream or downstream of the gene start or end, respectively. Motif signatures were obtained using the 'de novo' approach in Homer v4.7.2 (http://homer.ucsd.edu). The 'DESeq2' package in R was employed to identify differential gene expressions and accessibility with the threshold of absolute log2 FoldChange > log2 (1.5) and FDR ≤ 0.1. When a single gene was linked to multiple ATAC-seq peaks, all associated peaks were retained for analysis. A contingency plot was used to visualize the integrated results from ATAC-Seq and RNA-Seq data. Each quadrant in the plot indicates the statistical significance of either high or low expression for gene expression or accessibility.

Statistics and reproducibility

GraphPad 8 software and R were used for statistical analysis. Results were represented as means ± standard deviations (SDs). The normality of the population distribution will be assessed by Shapiro-Wilk test (a significance level of $\alpha = 0.05$) followed by visualizing with Q-Q plot or histogram. For *in vitro* studies, statistical significance between groups was performed by using an unpaired Student's t-test with a minimum of three biologically independent samples. For *in vivo* studies, between-group differences were assessed using the Mann-Whitney U test as a nonparametric method with a minimum of five biologically independent samples. Statistical significance was determined when p value was less than 0.05.

References

1. Early Breast Cancer Trialists' Collaborative G. Effects of chemotherapy and hormonal therapy for early breast cancer on recurrence and 15-year survival: an overview of the randomised trials. Lancet **2005**;365(9472):1687-717 doi 10.1016/S0140-6736(05)66544-0.
2. Giancotti FG. Mechanisms governing metastatic dormancy and reactivation. Cell **2013**;155(4):750-64 doi 10.1016/j.cell.2013.10.029.
3. Zhang XH, Giuliano M, Trivedi MV, Schiff R, Osborne CK. Metastasis dormancy in estrogen receptor-positive breast cancer. Clin Cancer Res **2013**;19(23):6389-97 doi 10.1158/1078-0432.CCR-13-0838.
4. Turajlic S, Swanton C. Metastasis as an evolutionary process. Science **2016**;352(6282):169-75 doi 10.1126/science.aaf2784.
5. Lambert AW, Pattabiraman DR, Weinberg RA. Emerging Biological Principles of Metastasis. Cell **2017**;168(4):670-91 doi 10.1016/j.cell.2016.11.037.
6. Gao H, Chakraborty G, Lee-Lim AP, Mavrakis KJ, Wendel HG, Giancotti FG. Forward genetic screens in mice uncover mediators and suppressors of metastatic reactivation. Proc Natl Acad Sci U S A **2014**;111(46):16532-7 doi 10.1073/pnas.1403234111.
7. Gao H, Chakraborty G, Lee-Lim AP, Mo Q, Decker M, Vonica A, *et al.* The BMP inhibitor Coco reactivates breast cancer cells at lung metastatic sites. Cell **2012**;150(4):764-79 doi 10.1016/j.cell.2012.06.035.
8. Gao H, Chakraborty G, Zhang Z, Akalay I, Gadiya M, Gao Y, *et al.* Multi-organ Site Metastatic Reactivation Mediated by Non-canonical Discoidin Domain Receptor 1 Signaling. Cell **2016**;166(1):47-62 doi 10.1016/j.cell.2016.06.009.
9. Su W, Han HH, Wang Y, Zhang B, Zhou B, Cheng Y, *et al.* The Polycomb Repressor Complex 1 Drives Double-Negative Prostate Cancer Metastasis by Coordinating Stemness and Immune Suppression. Cancer Cell **2019**;36(2):139-55 e10 doi 10.1016/j.ccell.2019.06.009.
10. Whyte WA, Orlando DA, Hnisz D, Abraham BJ, Lin CY, Kagey MH, *et al.* Master transcription factors and mediator establish super-enhancers at key cell identity genes. Cell **2013**;153(2):307-19 doi 10.1016/j.cell.2013.03.035.
11. El Khattabi L, Zhao H, Kalchschmidt J, Young N, Jung S, Van Blerkom P, *et al.* A Pliable Mediator Acts as a Functional Rather Than an Architectural Bridge between Promoters and Enhancers. Cell **2019**;178(5):1145-58 e20 doi 10.1016/j.cell.2019.07.011.
12. Verger A, Monte D, Villeret V. Twenty years of Mediator complex structural studies. Biochem Soc Trans **2019**;47(1):399-410 doi 10.1042/BST20180608.
13. Abdella R, Talyzina A, Chen S, Inouye CJ, Tjian R, He Y. Structure of the human Mediator-bound transcription preinitiation complex. Science **2021**;372(6537):52-6 doi 10.1126/science.abg3074.
14. Soutourina J. Transcription regulation by the Mediator complex. Nat Rev Mol Cell Biol **2018**;19(4):262-74 doi 10.1038/nrm.2017.115.
15. Allen BL, Taatjes DJ. The Mediator complex: a central integrator of transcription. Nat Rev Mol Cell Biol **2015**;16(3):155-66 doi 10.1038/nrm3951.
16. Ito M, Yuan CX, Okano HJ, Darnell RB, Roeder RG. Involvement of the TRAP220 component of the TRAP/SMCC coactivator complex in embryonic development and thyroid hormone action. Mol Cell **2000**;5(4):683-93 doi 10.1016/s1097-2765(00)80247-6.

17. Stevens JL, Cantin GT, Wang G, Shevchenko A, Shevchenko A, Berk AJ. Transcription control by E1A and MAP kinase pathway via Sur2 mediator subunit. Science **2002**;296(5568):755-8 doi 10.1126/science.1068943.
18. Barbieri CE, Baca SC, Lawrence MS, Demichelis F, Blattner M, Theurillat JP, *et al.* Exome sequencing identifies recurrent SPOP, FOXA1 and MED12 mutations in prostate cancer. Nat Genet **2012**;44(6):685-9 doi 10.1038/ng.2279.
19. Joung J, Konermann S, Gootenberg JS, Abudayyeh OO, Platt RJ, Brigham MD, *et al.* Genome-scale CRISPR-Cas9 knockout and transcriptional activation screening. Nat Protoc **2017**;12(4):828-63 doi 10.1038/nprot.2017.016.
20. Tsherniak A, Vazquez F, Montgomery PG, Weir BA, Kryukov G, Cowley GS, *et al.* Defining a Cancer Dependency Map. Cell **2017**;170(3):564-76 e16 doi 10.1016/j.cell.2017.06.010.
21. Cerami E, Gao J, Dogrusoz U, Gross BE, Sumer SO, Aksoy BA, *et al.* The cBio cancer genomics portal: an open platform for exploring multidimensional cancer genomics data. Cancer Discov **2012**;2(5):401-4 doi 10.1158/2159-8290.CD-12-0095.
22. Gao J, Aksoy BA, Dogrusoz U, Dresdner G, Gross B, Sumer SO, *et al.* Integrative analysis of complex cancer genomics and clinical profiles using the cBioPortal. Sci Signal **2013**;6(269):pl1 doi 10.1126/scisignal.2004088.
23. Lefebvre C, Bachelot T, Filleron T, Pedrero M, Campone M, Soria JC, *et al.* Mutational Profile of Metastatic Breast Cancers: A Retrospective Analysis. PLoS Med **2016**;13(12):e1002201 doi 10.1371/journal.pmed.1002201.
24. Siegel MB, He X, Hoadley KA, Hoyle A, Pearce JB, Garrett AL, *et al.* Integrated RNA and DNA sequencing reveals early drivers of metastatic breast cancer. J Clin Invest **2018**;128(4):1371-83 doi 10.1172/JCI96153.
25. Gyorffy B, Lanczky A, Eklund AC, Denkert C, Budczies J, Li Q, *et al.* An online survival analysis tool to rapidly assess the effect of 22,277 genes on breast cancer prognosis using microarray data of 1,809 patients. Breast Cancer Res Treat **2010**;123(3):725-31 doi 10.1007/s10549-009-0674-9.
26. Valastyan S, Weinberg RA. Tumor metastasis: molecular insights and evolving paradigms. Cell **2011**;147(2):275-92 doi 10.1016/j.cell.2011.09.024.
27. Pastushenko I, Blanpain C. EMT Transition States during Tumor Progression and Metastasis. Trends Cell Biol **2019**;29(3):212-26 doi 10.1016/j.tcb.2018.12.001.
28. De Cock JM, Shibue T, Dongre A, Keckesova Z, Reinhardt F, Weinberg RA. Inflammation Triggers Zeb1-Dependent Escape from Tumor Latency. Cancer Res **2016**;76(23):6778-84 doi 10.1158/0008-5472.CAN-16-0608.
29. Hnisz D, Abraham BJ, Lee TI, Lau A, Saint-Andre V, Sigova AA, *et al.* Super-enhancers in the control of cell identity and disease. Cell **2013**;155(4):934-47 doi 10.1016/j.cell.2013.09.053.
30. Mieczkowski J, Cook A, Bowman SK, Mueller B, Alver BH, Kundu S, *et al.* MNase titration reveals differences between nucleosome occupancy and chromatin accessibility. Nat Commun **2016**;7:11485 doi 10.1038/ncomms11485.
31. Ishihara S, Haga H. Matrix Stiffness Contributes to Cancer Progression by Regulating Transcription Factors. Cancers (Basel) **2022**;14(4) doi 10.3390/cancers14041049.
32. Paszek MJ, Zahir N, Johnson KR, Lakins JN, Rozenberg GI, Gefen A, *et al.* Tensional homeostasis and the malignant phenotype. Cancer Cell **2005**;8(3):241-54 doi 10.1016/j.ccr.2005.08.010.

33. Ueno H, Shinto E, Hashiguchi Y, Shimazaki H, Kajiwara Y, Sueyama T, *et al.* In rectal cancer, the type of desmoplastic response after preoperative chemoradiotherapy is associated with prognosis. Virchows Arch **2015**;466(6):655-63 doi 10.1007/s00428-015-1756-1.
34. Sun F, Sun T, Kronenberg M, Tan X, Huang C, Carey MF. The Pol II preinitiation complex (PIC) influences Mediator binding but not promoter-enhancer looping. Genes Dev **2021**;35(15-16):1175-89 doi 10.1101/gad.348471.121.
35. Wreggett KA, Hill F, James PS, Hutchings A, Butcher GW, Singh PB. A mammalian homologue of Drosophila heterochromatin protein 1 (HP1) is a component of constitutive heterochromatin. Cytogenet Cell Genet **1994**;66(2):99-103 doi 10.1159/000133676.
36. van Steensel B, Belmont AS. Lamina-Associated Domains: Links with Chromosome Architecture, Heterochromatin, and Gene Repression. Cell **2017**;169(5):780-91 doi 10.1016/j.cell.2017.04.022.
37. Reddy KL, Zullo JM, Bertolino E, Singh H. Transcriptional repression mediated by repositioning of genes to the nuclear lamina. Nature **2008**;452(7184):243-7 doi 10.1038/nature06727.
38. Peter M, Nakagawa J, Doree M, Labbe JC, Nigg EA. In vitro disassembly of the nuclear lamina and M phase-specific phosphorylation of lamins by cdc2 kinase. Cell **1990**;61(4):591-602 doi 10.1016/0092-8674(90)90471-p.
39. Heald R, McKeon F. Mutations of phosphorylation sites in lamin A that prevent nuclear lamina disassembly in mitosis. Cell **1990**;61(4):579-89 doi 10.1016/0092-8674(90)90470-y.
40. Janota CS, Calero-Cuenca FJ, Gomes ER. The role of the cell nucleus in mechanotransduction. Curr Opin Cell Biol **2020**;63:204-11 doi 10.1016/j.ceb.2020.03.001.
41. Medjkane S, Perez-Sanchez C, Gaggioli C, Sahai E, Treisman R. Myocardin-related transcription factors and SRF are required for cytoskeletal dynamics and experimental metastasis. Nat Cell Biol **2009**;11(3):257-68 doi 10.1038/ncb1833.
42. Egeblad M, Rasch MG, Weaver VM. Dynamic interplay between the collagen scaffold and tumor evolution. Curr Opin Cell Biol **2010**;22(5):697-706 doi 10.1016/j.ceb.2010.08.015.
43. Kechagia JZ, Ivaska J, Roca-Cusachs P. Integrins as biomechanical sensors of the microenvironment. Nat Rev Mol Cell Biol **2019**;20(8):457-73 doi 10.1038/s41580-019-0134-2.
44. Case LB, Waterman CM. Integration of actin dynamics and cell adhesion by a three-dimensional, mechanosensitive molecular clutch. Nat Cell Biol **2015**;17(8):955-63 doi 10.1038/ncb3191.
45. Jones SF, Siu LL, Bendell JC, Cleary JM, Razak AR, Infante JR, *et al.* A phase I study of VS-6063, a second-generation focal adhesion kinase inhibitor, in patients with advanced solid tumors. Invest New Drugs **2015**;33(5):1100-7 doi 10.1007/s10637-015-0282-y.
46. Keenan AB, Torre D, Lachmann A, Leong AK, Wojciechowicz ML, Utti V, *et al.* ChEA3: transcription factor enrichment analysis by orthogonal omics integration. Nucleic Acids Res **2019**;47(W1):W212-W24 doi 10.1093/nar/gkz446.
47. Esnault C, Stewart A, Gualdrini F, East P, Horswell S, Matthews N, *et al.* Rho-actin signaling to the MRTF coactivators dominates the immediate transcriptional response to serum in fibroblasts. Genes Dev **2014**;28(9):943-58 doi 10.1101/gad.239327.114.

48. Cordenonsi M, Zanconato F, Azzolin L, Forcato M, Rosato A, Frasson C, *et al.* The Hippo transducer TAZ confers cancer stem cell-related traits on breast cancer cells. Cell **2011**;147(4):759-72 doi 10.1016/j.cell.2011.09.048.
49. Zhao B, Ye X, Yu J, Li L, Li W, Li S, *et al.* TEAD mediates YAP-dependent gene induction and growth control. Genes Dev **2008**;22(14):1962-71 doi 10.1101/gad.1664408.
50. Posern G, Treisman R. Actin' together: serum response factor, its cofactors and the link to signal transduction. Trends Cell Biol **2006**;16(11):588-96 doi 10.1016/j.tcb.2006.09.008.
51. Calvo F, Ege N, Grande-Garcia A, Hooper S, Jenkins RP, Chaudhry SI, *et al.* Mechanotransduction and YAP-dependent matrix remodelling is required for the generation and maintenance of cancer-associated fibroblasts. Nat Cell Biol **2013**;15(6):637-46 doi 10.1038/ncb2756.
52. Foster CT, Gualdrini F, Treisman R. Mutual dependence of the MRTF-SRF and YAP-TEAD pathways in cancer-associated fibroblasts is indirect and mediated by cytoskeletal dynamics. Genes Dev **2017**;31(23-24):2361-75 doi 10.1101/gad.304501.117.
53. Dupont S, Morsut L, Aragona M, Enzo E, Giulitti S, Cordenonsi M, *et al.* Role of YAP/TAZ in mechanotransduction. Nature **2011**;474(7350):179-83 doi 10.1038/nature10137.
54. Yin JW, Wang G. The Mediator complex: a master coordinator of transcription and cell lineage development. Development **2014**;141(5):977-87 doi 10.1242/dev.098392.
55. Rasool RU, Natesan R, Deng Q, Aras S, Lal P, Sander Effron S, *et al.* CDK7 Inhibition Suppresses Castration-Resistant Prostate Cancer through MED1 Inactivation. Cancer Discov **2019**;9(11):1538-55 doi 10.1158/2159-8290.CD-19-0189.
56. Yang Y, Leonard M, Zhang Y, Zhao D, Mahmoud C, Khan S, *et al.* HER2-Driven Breast Tumorigenesis Relies upon Interactions of the Estrogen Receptor with Coactivator MED1. Cancer Res **2018**;78(2):422-35 doi 10.1158/0008-5472.CAN-17-1533.
57. Tsang FH, Law CT, Tang TC, Cheng CL, Chin DW, Tam WV, *et al.* Aberrant Super-Enhancer Landscape in Human Hepatocellular Carcinoma. Hepatology **2019**;69(6):2502-17 doi 10.1002/hep.30544.
58. Lyng H, Lando M, Brovig RS, Svendsrud DH, Johansen M, Galteland E, *et al.* GeneCount: genome-wide calculation of absolute tumor DNA copy numbers from array comparative genomic hybridization data. Genome Biol **2008**;9(5):R86 doi 10.1186/gb-2008-9-5-r86.
59. Albrecht P, Ansperger-Rescher B, Schuler A, Zeschnigk M, Gallie B, Lohmann DR. Spectrum of gross deletions and insertions in the RB1 gene in patients with retinoblastoma and association with phenotypic expression. Hum Mutat **2005**;26(5):437-45 doi 10.1002/humu.20234.
60. Mitter D, Ullmann R, Muradyan A, Klein-Hitpass L, Kanber D, Ounap K, *et al.* Genotype-phenotype correlations in patients with retinoblastoma and interstitial 13q deletions. Eur J Hum Genet **2011**;19(9):947-58 doi 10.1038/ejhg.2011.58.
61. Dechat T, Pfleghaar K, Sengupta K, Shimi T, Shumaker DK, Solimando L, *et al.* Nuclear lamins: major factors in the structural organization and function of the nucleus and chromatin. Genes Dev **2008**;22(7):832-53 doi 10.1101/gad.1652708.
62. Tajik A, Zhang Y, Wei F, Sun J, Jia Q, Zhou W, *et al.* Transcription upregulation via force-induced direct stretching of chromatin. Nat Mater **2016**;15(12):1287-96 doi 10.1038/nmat4729.

63. Iyer KV, Pulford S, Mogilner A, Shivashankar GV. Mechanical activation of cells induces chromatin remodeling preceding MKL nuclear transport. Biophys J **2012**;103(7):1416-28 doi 10.1016/j.bpj.2012.08.041.
64. Sun J, Chen J, Mohagheghian E, Wang N. Force-induced gene up-regulation does not follow the weak power law but depends on H3K9 demethylation. Sci Adv **2020**;6(14):eaay9095 doi 10.1126/sciadv.aay9095.
65. Olson EN, Nordheim A. Linking actin dynamics and gene transcription to drive cellular motile functions. Nat Rev Mol Cell Biol **2010**;11(5):353-65 doi 10.1038/nrm2890.
66. O'Connor JW, Riley PN, Nalluri SM, Ashar PK, Gomez EW. Matrix Rigidity Mediates TGFbeta1-Induced Epithelial-Myofibroblast Transition by Controlling Cytoskeletal Organization and MRTF-A Localization. J Cell Physiol **2015**;230(8):1829-39 doi 10.1002/jcp.24895.
67. Buyukcelebi K, Chen X, Abdula F, Elkafas H, Duval AJ, Ozturk H, *et al.* Engineered MED12 mutations drive leiomyoma-like transcriptional and metabolic programs by altering the 3D genome compartmentalization. Nat Commun **2023**;14(1):4057 doi 10.1038/s41467-023-39684-y.
68. Berry DA, Cronin KA, Plevritis SK, Fryback DG, Clarke L, Zelen M, *et al.* Effect of screening and adjuvant therapy on mortality from breast cancer. N Engl J Med **2005**;353(17):1784-92 doi 10.1056/NEJMoa050518.
69. Aslakson CJ, Miller FR. Selective events in the metastatic process defined by analysis of the sequential dissemination of subpopulations of a mouse mammary tumor. Cancer Res **1992**;52(6):1399-405.
70. Pelossof R, Fairchild L, Huang CH, Widmer C, Sreedharan VT, Sinha N, *et al.* Prediction of potent shRNAs with a sequential classification algorithm. Nat Biotechnol **2017**;35(4):350-3 doi 10.1038/nbt.3807.
71. Nguyen-Ngoc KV, Shamir ER, Huebner RJ, Beck JN, Cheung KJ, Ewald AJ. 3D culture assays of murine mammary branching morphogenesis and epithelial invasion. Methods Mol Biol **2015**;1189:135-62 doi 10.1007/978-1-4939-1164-6_10.
72. Bae SY, Kim HJ, Lee KJ, Lee K. Translationally controlled tumor protein induces epithelial to mesenchymal transition and promotes cell migration, invasion and metastasis. Sci Rep **2015**;5:8061 doi 10.1038/srep08061.
73. Cheng L, Zhang X, Wang Y, Gan H, Xu X, Lv X, *et al.* Chromatin Assembly Factor 1 (CAF-1) facilitates the establishment of facultative heterochromatin during pluripotency exit. Nucleic Acids Res **2019**;47(21):11114-31 doi 10.1093/nar/gkz858.
74. Dobin A, Davis CA, Schlesinger F, Drenkow J, Zaleski C, Jha S, *et al.* STAR: ultrafast universal RNA-seq aligner. Bioinformatics **2013**;29(1):15-21 doi 10.1093/bioinformatics/bts635.
75. Anders S, Pyl PT, Huber W. HTSeq--a Python framework to work with high-throughput sequencing data. Bioinformatics **2015**;31(2):166-9 doi 10.1093/bioinformatics/btu638.
76. Love MI, Huber W, Anders S. Moderated estimation of fold change and dispersion for RNA-seq data with DESeq2. Genome Biol **2014**;15(12):550 doi 10.1186/s13059-014-0550-8.
77. Subramanian A, Tamayo P, Mootha VK, Mukherjee S, Ebert BL, Gillette MA, *et al.* Gene set enrichment analysis: a knowledge-based approach for interpreting genome-wide expression profiles. Proc Natl Acad Sci U S A **2005**;102(43):15545-50 doi 10.1073/pnas.0506580102.

78. Buenrostro JD, Giresi PG, Zaba LC, Chang HY, Greenleaf WJ. Transposition of native chromatin for fast and sensitive epigenomic profiling of open chromatin, DNA-binding proteins and nucleosome position. Nat Methods **2013**;10(12):1213-8 doi 10.1038/nmeth.2688.

Acknowledgments

This study is dedicated to the memory of our mentor, teacher, and friend, Filippo Giancotti, a pioneer in the metastasis field known for his brilliance, rigor, and kindness. This work was supported by NIH grant R35 CA197566 and partially by CPRIT Recruitment of Established Investigators Award RR160031 (F.G.G.). Use of the Core Facilities was supported by NIH grants P30CA008748 (MSKCC), P30 CA016672 (MDACC), and P30 CA013696 (Columbia University).

Author's Contributions

S. Bae: Conceptualization, validation, investigation, methodology, writing-original draft, writing-review and editing. **F.G. Giancotti:** Conceptualization, funding acquisition **Y. Chen:** Formal analysis and validation. **H. Chen:** Formal analysis and validation. **S. Karaiskos:** Formal analysis and validation. **A.D. Viny:** Validation, investigation, writing-original draft, writing-review and editing.

Figure Legends

Figure 1. *Med4* was identified as a gatekeeper for metastatic reactivation by forward genetic screening using CRISPR-Cas9 system. A, Schematic representation of the *in vivo* CRISPR-Cas9 screening strategy. **B,** The scheme of chromatin looping for enhancer-promoter interaction. **C,** RT-qPCR analysis and immunoblots of *Med4* expression in D2A1-d-TGL cells expressing MirE shRNA targeting either non-targeting control (NTC) or *Med4*; Mean values (± S.D.) p values; unpaired Student's t-test. **D-F,** D2A1-d-TGL cells transduced with either NTC or *Med4* shRNAs were inoculated *i.v.* in syngeneic mice. Lung metastasis was measured by bioluminescent (BLI) imaging at the indicated time. The panels show representative images (D), the graphs of the normalized BLI photon flux (E), and the graphs of the counts of macrometastases (F). Mean values (± S.D.) p values; Mann-Whitney U test (E and F). **G-J,** Schematic representation of inducible expression experiment (G), Immunoblot analysis of MED4 in D2A1-d-TGL cells transduced with doxycycline (Dox)-inducible MirE shRNA targeting NTC or *Med4* (H), D2A1-d-TGL cells expressing Dox-inducible MirE shRNA targeting NTC or *Med4* were inoculated *i.v.* in syngeneic mice. Dox was administrated either immediately after injection (Dox day 0) or 14 days after inoculation of the cells (Dox day 14). Lung metastasis was measured by BLI normalized photon flux at the indicated time. The panels show representative images (I), and the graphs of the normalized BLI photon flux (J); Mean values (± S.D.) p values; Mann-Whitney U test. **K,** Copy number alterations in metastatic breast cancer patients (from INSERM) were analyzed by cBioportal database. **L,** *MED4* mRNA levels were measured by paired RNA-seq of primary tumors and multiple metastases. **M,** Kaplan-Meier analysis of relapse-free survival (RFS) of all patients in publicly available breast cancer datasets (source KM Plotter for breast cancer). Patients were stratified according to *MED4* expression using a probe set, 222438_at as indicated. HR, hazard ratio.

Figure 2. The downregulation of *Med4* leads to the reprogramming of the transcriptional and epigenetic landscape, bolstering matrix stiffening. A, Heatmap of differentially expressed genes (DEGs; |Fold change| ≥ 2, FDR < 0.05) in NTC versus *Med4*-silenced D2A1-d-TGL cells. **B,** MNase digestion assay was performed in nuclei isolated from the indicated cells for increasing incubation time. The panels show the representative image (upper), and the quantification graph (lower). **C,** Differential accessibility ($\log_2$ fold change in reads per accessible region) plotted against the mean reads per region. **D,** Intersection of RNA-seq and ATAC-seq plotted as $-\log_{10}$(FDR)*sign of the $\log_2$ fold change of *Med4*-sileced D2A1-d-TGL cells compared to NTC and each point representing one ATAC peak. **E,** Gene ontology (GO) analysis of the genes located in the upper quadrant of (D) from the intersection of RNA-seq and ATAC-seq. **F,** Heatmap shows the expression level of matrisome genes amongst the top differentially expressed genes in NTC versus *Med4*-depleted cells. **G,** Immunohistochemistry for α-SMA and Masson's trichrome staining on lung metastases in mice that were intravenously injected with D2A1-d-TGL cells transduced with either non-targeting control (NTC) or *Med4* shRNAs.

Figure 3. *Med4* silencing decompacts 3D chromatin structure by pulling on the nuclear lamina through stress fibers. A, D2A1-d cells expressing either NTC or *Med4* shRNAs were stained with HP1α (red). The panels display representative images (left) and fluorescence intensity profiles across one cell (right). **B,** Cells were co-stained with H3K9me3 (red) and

LAMIN A/C (green). The panels show representative images (left) and fluorescence intensity profile of H3K9me3 across one cell (right). **C** and **D,** D2A1-d cells expressing either NTC or *Med4* shRNAs were co-transduced with either empty vector (EV) or Flag-HA tagged MED4 cDNA to rescue MED4 expression. Immunoblots of MED4 and HA (C). Cells were stained with LAMIN A/C (red) and nuclei were counter-stained with DAPI (blue). The panel shows representative images (left) and quantification of nucleus sizes in diameter (right) (D); Mean values (± S.D.) p values; unpaired Student's t-test. **E,** D2A1-d cells expressing either NTC or *Med4* shRNAs were treated with 0.1% DMSO, 200 nM cytochalasin D, or 100 nM latrunculin B for 20 min as indicated. Cells were stained with LAMIN A/C (green) and F-actin (red). Nuclei were counter-stained with DAPI (blue). The panel shows representative images (left) and quantification of nucleus sizes in volume (right); Mean values (± S.D.) p values; unpaired Student's t-test. **F,** D2A1-d cells expressing either NTC or *Med4* shRNAs were treated with 0.1% DMSO or 200 nM cytochalasin D for 20 min. Cells were stained with HP1α (red) and F-actin (green). The panels show representative images (left) and fluorescence intensity profile of HP1α across one cell (right).

Figure 4. *Med4*-deficient cells exhibit a propensity to grow within a desmoplastic niche, through the activation of integrin signaling. A, D2A1-d cells expressing MirE shRNA targeting *Med4* or NTC were cultured on 3D Matrigel with or without collagen I. **B,** Cells were cultured either on 2D or on 3D Matrigel + collagen I matrix, and stained with Ki67 (purple). Nuclei were counterstained with DAPI (blue). The panel shows representative images (top) and quantification graphs for numbers of Ki67+ cells (bottom). **C,** D2A1-d cells expressing MirE shRNA targeting Med4 cultured on 2D were stained for focal adhesions, and the nuclei were stained with DAPI (blue). **D,** Total cell lysates were subjected to immunoblotting for integrin-signaling molecules. **E,** D2A1-d cells expressing either NTC or Med4 shRNAs were cultured either on 3D Matrigel + collagen I matrix, and stained with either F-actin or p-FAK (Y^{397}). Nuclei were counter-stained with DAPI. **F,** D2A1-d cells treated with or without 2.5 μM defactinib were cultured either on 3D Matrigel + collagen I matrix.

Figure 5. *Med4* loss activates integrin-mediated mechano-transduction MRTF/SRF and YAP/TAZ pathways. A, ChEA3 TF enrichment analysis of the promoters of the genes upregulated in *Med4*-deficient cells compared to NTC. **B,** HOMER motif analysis of genes in the upper right quadrant of (Figure 2D) which represents the intersection of RNA-seq and ATAC-seq data in *Med4*-silenced D2A1-d-TGL cells compared to non-targeting control (NTC). p-values were generated using the binomial test. **C,** Gene signature enrichment analysis (GSEA) of MRTF, SRF, and YAP transcriptional signatures. NES, normalized enrichment score; FDR, false discovery rate (n = 3 biological replicates per condition). **D,** D2A1-d cells expressing MirE shRNA targeting *Med4* cultured on 2D were stained for MRTF-A (red), or for YAP (purple). The nuclei were counterstained with DAPI (blue). **E** and **F,** D2A1-d cells expressing either NTC or *Med4* shRNAs were co-transduced with either empty vector (EV) or Flag-HA tagged MED4 cDNA to rescue MED4 expression. Cells were stained with MRTF-A (red) and counter-stained with DAPI (blue). The panel shows representative images (E) and quantification of subcellular localization (F). **G,** D2A1-d-TGL cells co-transduced with indicated MirE shRNAs were inoculated *i.v.* in syngeneic mice. Lung metastasis was measured by bioluminescent (BLI) imaging at the indicated time. The panels show representative images (left), and the graphs of the normalized BLI photon flux (right). Mean values (± S.D.) p values; Mann-Whitney U test.

Supplemental figure Legends

Supplementary Figure S1. *Med4* was hemizygously deleted to induce metastatic reactivation.

(A) 4T07-TGL cells either mock control or expressing GeCKO v2 library were inoculated *i.v.* into BALB/c syngeneic mice. Lung metastasis was measured by bioluminescent (BLI) imaging at the indicated time.

(B) Schematics of the mouse chromosomal region encompassing *Med4*, location of the sequence complementary to the gRNA isolated from the screening, and the primer pairs used for genomic DNA PCR.

(C) The isolated clone from the screening which harbors a gRNA targeting *Med4* was subjected to an indel analysis using genomic DNA PCR (left) and immunoblotting (right).

(D) Sequences of the fragments of DNA deleted by CRISPR-Cas9. Red boxes indicate the junction. (E) Sequence alignment results of translated amino acids from each allele to wild type MED4.

(F) DepMap analysis of the dependency of tumor cell line panels in CRISPR (blue) and RNAi (violet) databases on MED4. X-axis: dependency scores.

(G) RT-qPCR analysis of *Med4* expression in 4T07-TGL cells expressing MirE shRNA targeting either non-targeting control (NTC) or *Med4*; Mean values (± S.D.) p-values; unpaired Student's t-test.

(H and I) 4T07-TGL cells transduced with either NTC or *Med4* shRNAs were inoculated *i.v.* in syngeneic mice. Lung metastasis was measured by bioluminescent (BLI) imaging at the indicated time. The panels show representative images (H), and the graphs of the normalized BLI photon flux (I). Mean values (± S.D.) p values; Mann-Whitney U test.

Supplementary Figure S2. *MED4* loss serves as a predictor for breast cancer relapse.

(A and B) cBioportal analysis of copy number alterations in metastatic breast cancer patients from the Metastatic Breast Cancer Project; Provisional (A) and Archived (B).

(C) Kaplan-Meier analysis of RFS in patients stratified according to *MED4* expression using a probe set, 222438_at as indicated. Patients were subdivided by breast cancer subtypes according to PAM50.

(D and E) Kaplan-Meier analysis of RFS in patients stratified according to *MED4* expression using a probe set, 222438_at as indicated. Patients were subdivided by estrogen receptor (ER) expression level (D) or by human epidermal growth factor receptor 2 (*HER2*) expression level determined by Affymetrix microarray (E).

(F and G) KM plotter analysis of overall survival (OS) based on *MED4* expression level from RNA-seq data of breast cancer patients. Patients were subdivided by estrogen receptor (ER) expression level (F) or by human epidermal growth factor receptor 2 (*HER2*) expression level determined by Affymetrix microarray (G). HR, hazard ratio.

Supplementary Figure S3. *Med4* depletion promotes cancer stem cell traits in D2A1-d cells.

(A) Cell growth of D2A1-d-TGL cells expressing MirE shRNA targeting either NTC or *Med4* was measured by counting cell numbers at the indicated time; Mean values (± S.D.) p values; unpaired Student's t-test (n = 3 per group, *P = 0.0171, **P = 0.0017, ***P = 0.0004).

(B) Control or Med4-silenced D2A1-d-TGL cells were subjected to tumorsphere assay. The panel shows representative images of wells and microscopic images of tumor spheres (left) and

mean numbers of organoid (± S.D.; right) per 10,000 cells. p values; unpaired Student's t-test (n = 3 per group, *P = 0.0122, **P = 0.0089).
(C) Indicated D2A1-d-TGL cells were subjected to clonogenicity assay. The panel shows representative images of dishes and microscopic images of colonies (left) and mean numbers of colonies (± S.D.; right) per 1,000 cells. p values; unpaired Student's t-test (n = 3 per group, **P = 0.0056, ***P = 0.0006).
(D) Indicated D2A1-d-TGL cells were subjected to soft agar assay. The panel shows representative images of wells and microscopic images of colonies (left) and mean numbers of colonies (± S.D.; right) per 10,000 cells. p values; unpaired Student's t-test (n = 3 per group, *P = 0.0118, ****P < 0.0001).
(E and F) Control or *Med4*-silenced D2A1-d-TGL cells were subjected to transwell migration assay (E) and transwell invasion assay (F). The panel shows representative images of fields (left) and mean numbers of cells (± S.D.; right) per field. p values; unpaired Student's t-test ((E) n = 3 per group, ***P = 0.0007, ***P = 0.0009, (F) n = 3 per group, **P = 0.0018, ***P = 0.0007).

Supplementary Figure S4. *Med4* depletion promotes cancer stem cell traits in 4T07 cells.
(A) Cell growth of 4T07-TGL cells expressing MirE shRNA targeting either NTC or *Med4* was measured by counting cell numbers at the indicated time; Mean values (± S.D.) p values; unpaired Student's t-test (n = 3 per group, **P = 0.0040, **P = 0.0067, ***P = 0.0003).
(B) Tumorsphere assay results in control and *Med4*-silenced 4T07-TGL cells. The panel shows representative images of wells and microscopic images of tumor spheres (left) and mean numbers of organoid (± S.D.; right) per 10,000 cells. p values; unpaired Student's t-test (n = 3 per group, *P = 0.0158, **P = 0.0055).
(C) Clonogenicity assay results in control and *Med4*-depleted 4T07-TGL. The panel shows representative images of dishes and microscopic images of colonies (left) and mean numbers of colonies (± S.D.; right) per 1,000 cells. p values; unpaired Student's t-test (n = 3 per group, ***P = 0.0002, ****P < 0.0001).
(D) Soft agar assay results in the indicated 4T07-TGL cells. The panel shows representative images of wells and microscopic images of colonies (left) and mean numbers of colonies (± S.D.; right) per 1,000 cells. p values; unpaired Student's t-test (n = 3 per group, **P = 0.0018, **P = 0.0027). (E) Transwell migration results of control and *Med4*-silenced 4T07-TGL cells. The panel shows representative images of fields (left) and mean numbers of cells (± S.D.; right) per field. p values; unpaired Student's t-test (n = 3 per group, ***P = 0.0001, ****P < 0.0001).

Supplementary Figure S5. *Med1* alters the transcriptional and epigenetic landscape discordantly with *Med4* while *Med4*-loss driven transcriptional program is necessary for metastasis.
(A) MA plot from RNA-seq analysis in D2A1 versus D2A1-d cells (Fold change ≥ 2, FDR < 0.05)
(B) GSEA plots of D2A1_metastatic and D2A1_dormant signatures in Med4-depleted cells as compared with control cells.
(C) RT-qPCR analysis and immunoblots of *Med1* expression in D2A1-d-TGL cells expressing MirE shRNA targeting either non-targeting control (NTC) or *Med1*; Mean values (± S.D.) p values; unpaired Student's t-test.
(D) Heatmap of differentially expressed genes (DEGs; Fold change ≥ 2, FDR < 0.05) in NTC versus *Med1*-silenced D2A1-d-TGL cells.

(E) GSEA plots of D2A1_metastatic and D2A1_dormant signatures in *Med1*-silenced cells as compared with control cells.
(F) The heatmap showing the $\log_2$ fold change (Log2FC) in the gene expression of selected Mediator subunits when comparing sh*Med1* and *shMed4* to NTC, respectively. Each cell in the heatmap contains a numerical value representing the Log_2FC, rounded to one decimal place.
(G) RT-qPCR analysis of *Med4* and *Med1* expression in D2A1-d-TGL cells expressing MirE shRNA targeting either non-targeting control (NTC) or *Med4*; Mean values (± S.D.) p values; unpaired Student's t-test.
(H) RT-qPCR analysis of *Med4* and *Med1* expression in D2A1-d-TGL cells expressing MirE shRNA targeting either non-targeting control (NTC) or *Med1*; Mean values (± S.D.) p values; unpaired Student's t-test.
(I) MNase digestion assay was performed in nuclei isolated from the indicated cells for increasing incubation time. The panels show the representative image (upper), and the quantification graph (lower).
(J) MA plot of ATAC-seq results comparing NTC versus *Med1*-silenced D2A1-d-TGL cells. Differential accessibility ($\log_2$ fold change in reads per accessible region) plotted against the mean reads per region.
(K) The dot plot represents the gene set enrichment analysis (GSEA) across four datasets (Hallmarks, KEGG, Reactome, and GO). The indicated pathways were enriched in *Med4*-silenced D2A1-d cells.
(L) GSEA plots show enrichment of HALLMARK_EMT, REACTOME_ECM organization, and KEGG_Focal adhesion in NTC versus sh*Med4*.

Supplementary Figure S6. The downregulation of *Med1* did not produce discordant alterations in nuclear and chromatin structure, in contrast to the effects observed with *Med4* silencing.
(A) D2A1-d cells expressing either NTC or *Med1* shRNAs were stained with HP1α (red). The panels show representative images (left) and fluorescence intensity profile across one cell (right).
(B) Cells were stained with LAMIN A/C (red) and counter-stained with DAPI (blue).
(C) D2A1-d cells expressing either NTC or Med4 shRNAs were subcellular fractionized into the cytoplasm, nucleoplasm, and nuclear envelope (NE). Total lysates were subsequently analyzed by immunoblotting using the indicated antibodies.
(D) D2A1-d cells expressing either NTC or *Med4* shRNAs were treated with 100 nM Latrunculin B for 20 min. Cells were stained with HP1α (red) and F-actin (green). The panels show representative images (left) and fluorescence intensity profile of HP1α across one cell (right).

Supplementary Figure S7. Med4 alters the repertoire of integrin subunits and mediates the signaling pathway of integrin-mediated mechano-transduction.
(A) A GSEA plot of integrin complex (GO_CC; top). Heatmap shows the level of expression of integrin subunit genes amongst the top differentially expressed genes in control versus *Med4*-silenced D2A1-d-TGL cells (bottom).
(B) RT-qPCR results were indicated as relative mean expression of MRTF/SRF only target genes, YAP only target genes and shared target genes in either control or Med4-silenced D2A1-d cells. (C) RT-qPCR results were indicated as relative mean expression of MRTF/SRF only target genes in D2A1-d cells expressing either NTC or Med4 shRNAs were co-transduced with either

empty vector (EV) or Flag-HA tagged MED4 cDNA. p values; unpaired Student's t-test (n = 3 per group, *P = 0.0449, **P = 0.0016, ***P = 0.001, ****P < 0.0001).

(D) D2A1-d-TGL cells transduced with either NTC or Med4 shRNAs were inoculated *i.v.* in syngeneic mice. Lung sections were stained as indicated.

(E) D2A1-d-TGL cells were co-transduced with MirE shRNA targets for Med4 and MirE shRNA targets the mechanosensitive transcription factors as indicated. Total lysates were subjected to immunoblotting with the indicated antibodies.

Figure 1 Bae et al.

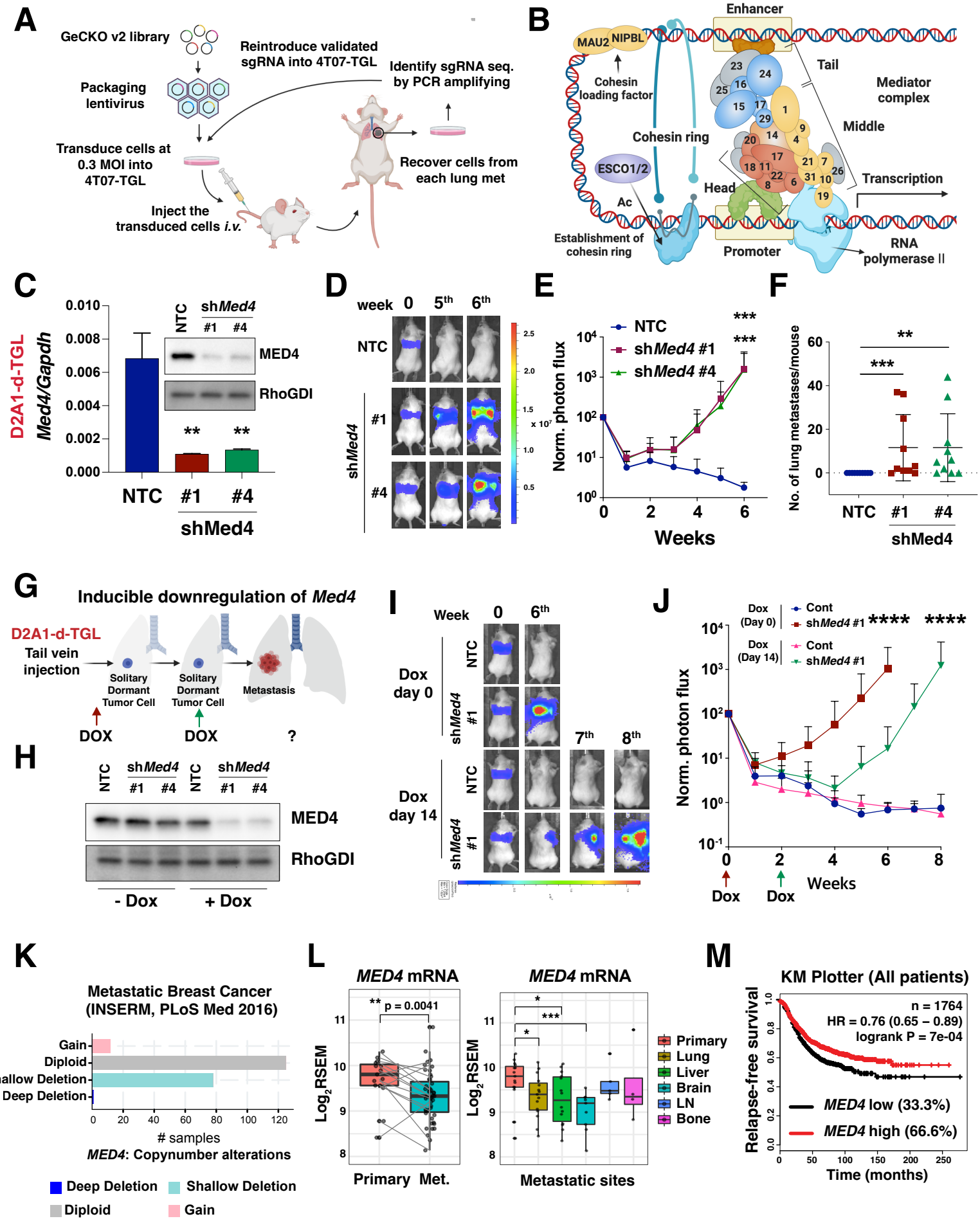

Figure 2 Bae et al.

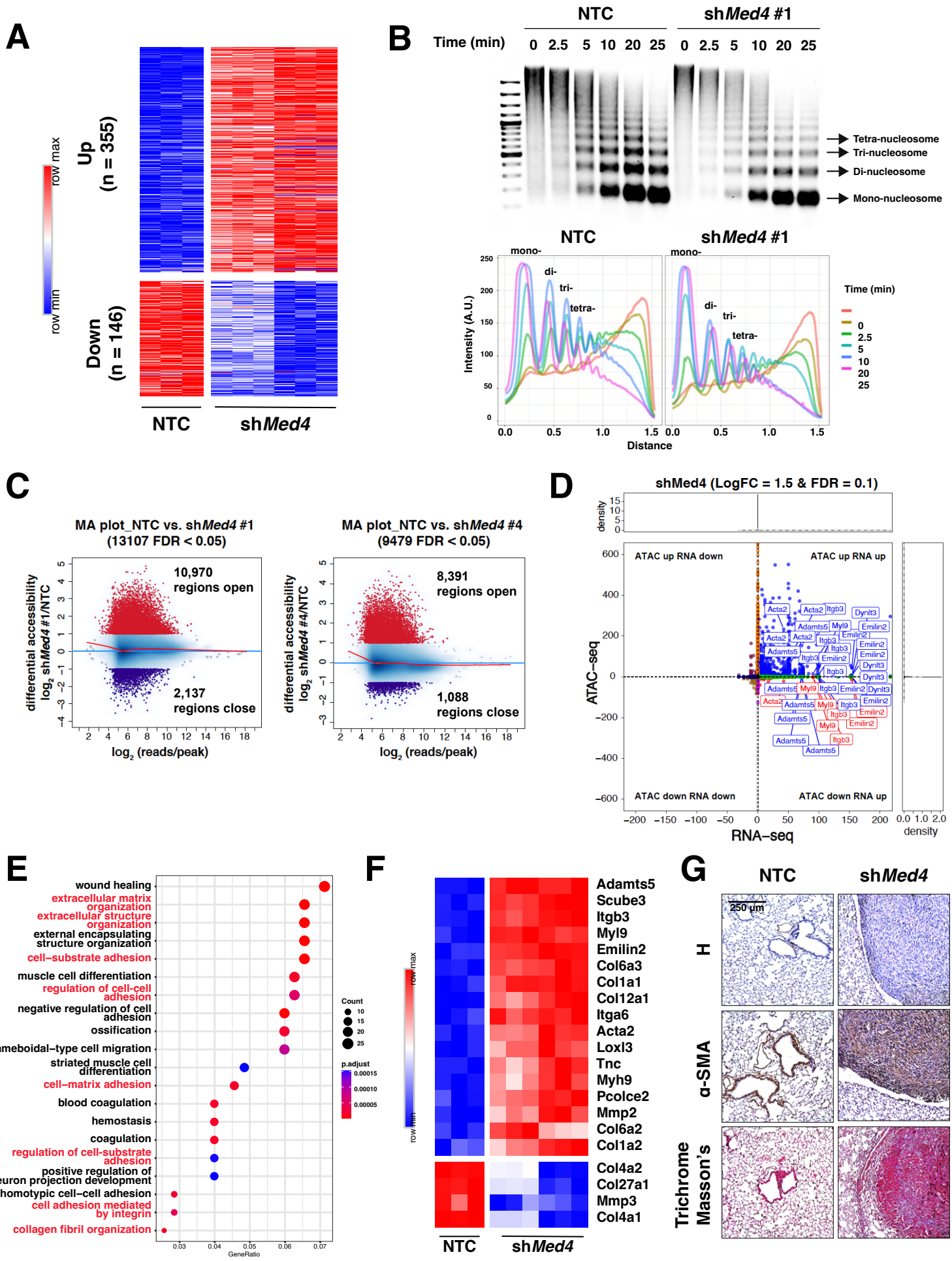

Figure 3 Bae et al.

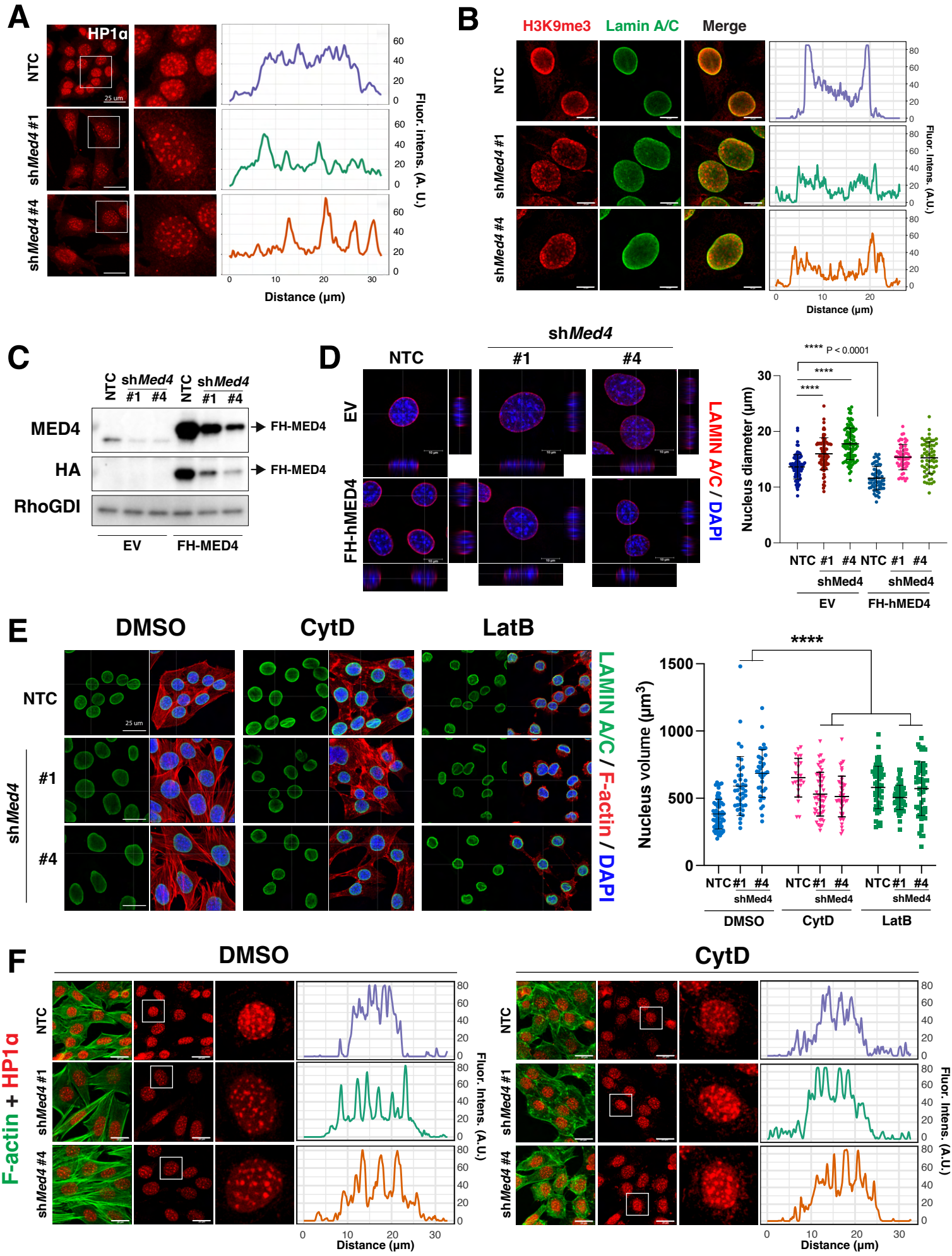

Figure 4 Bae et al.

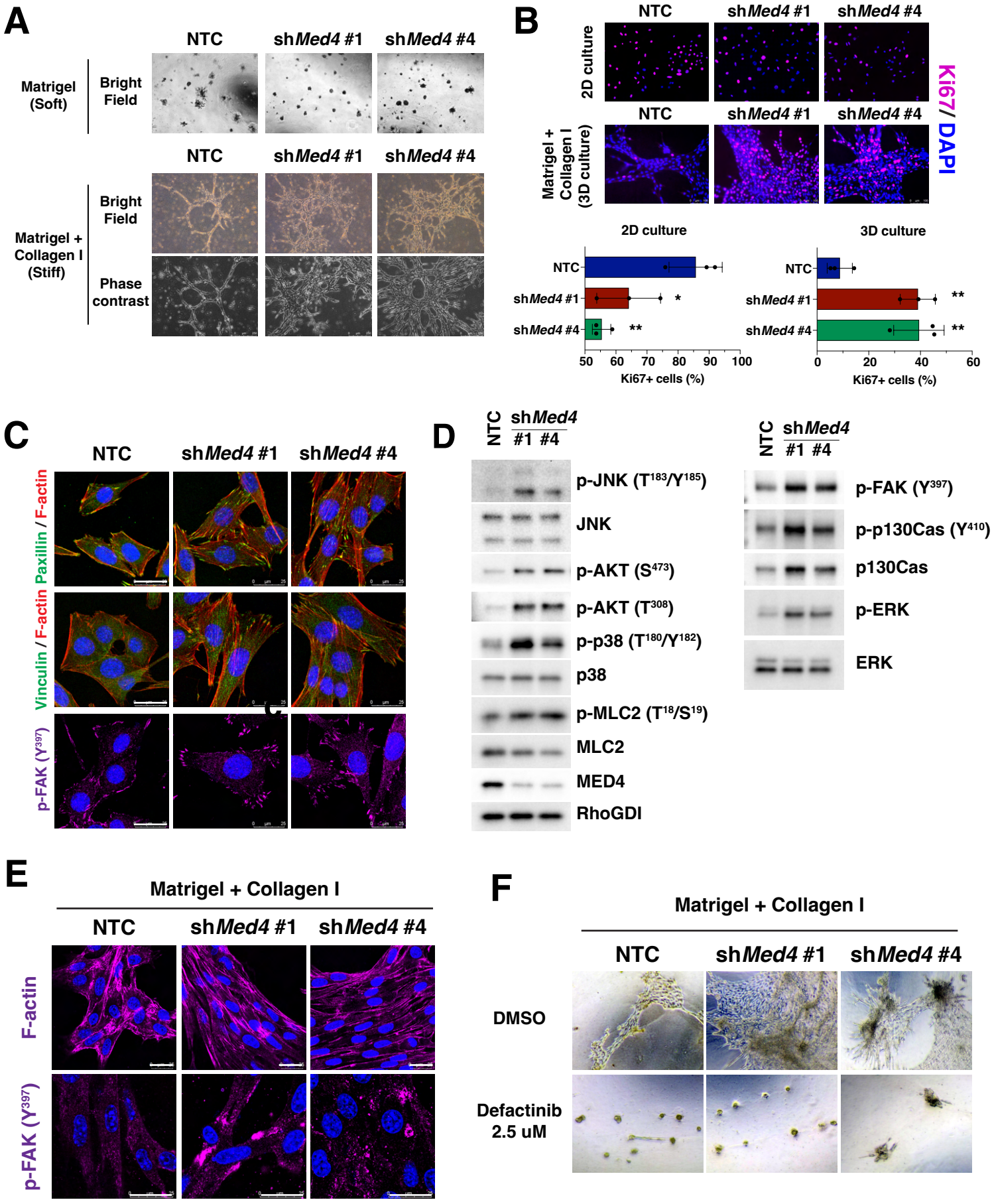

Figure 5 Bae et al.

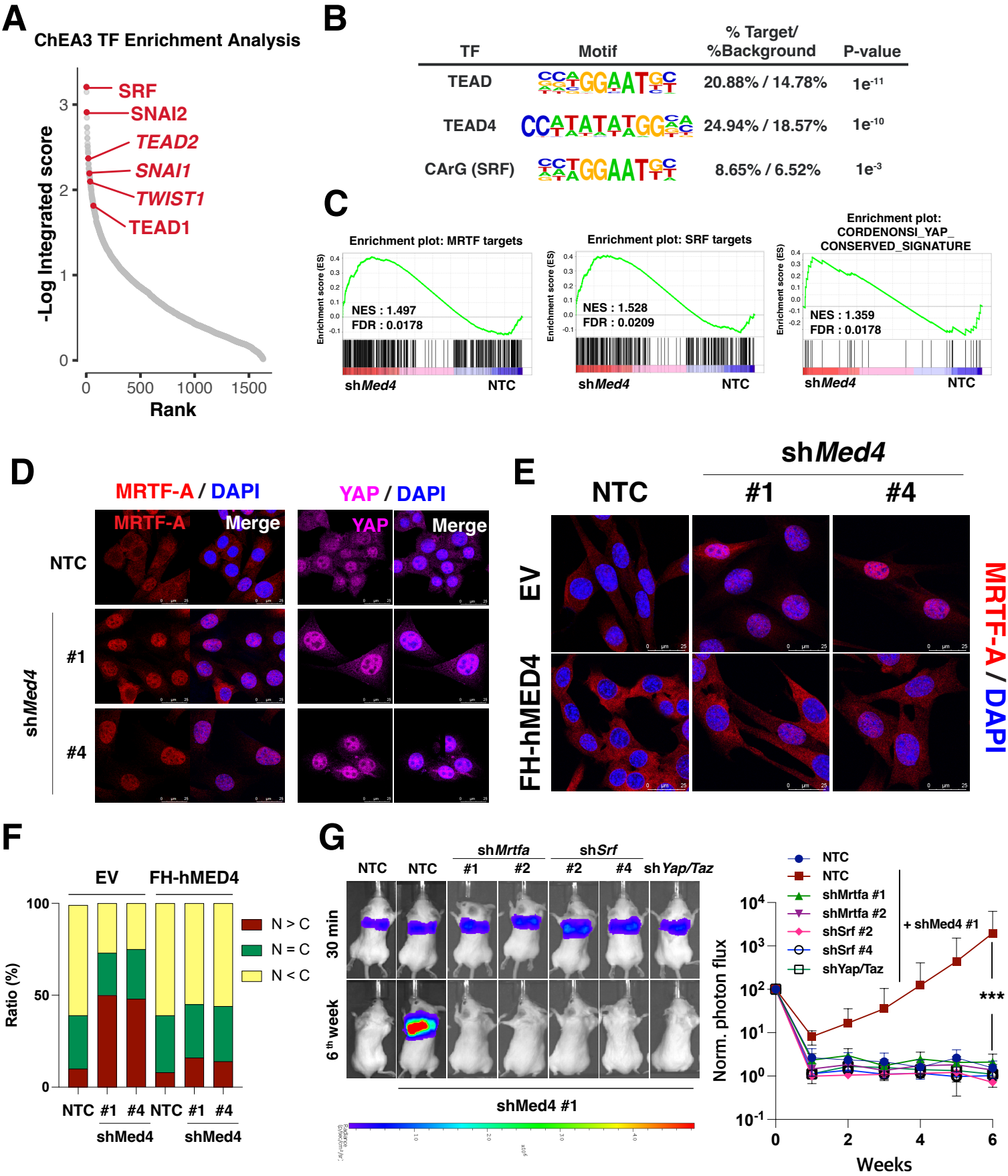

Figure S1 Bae et al.

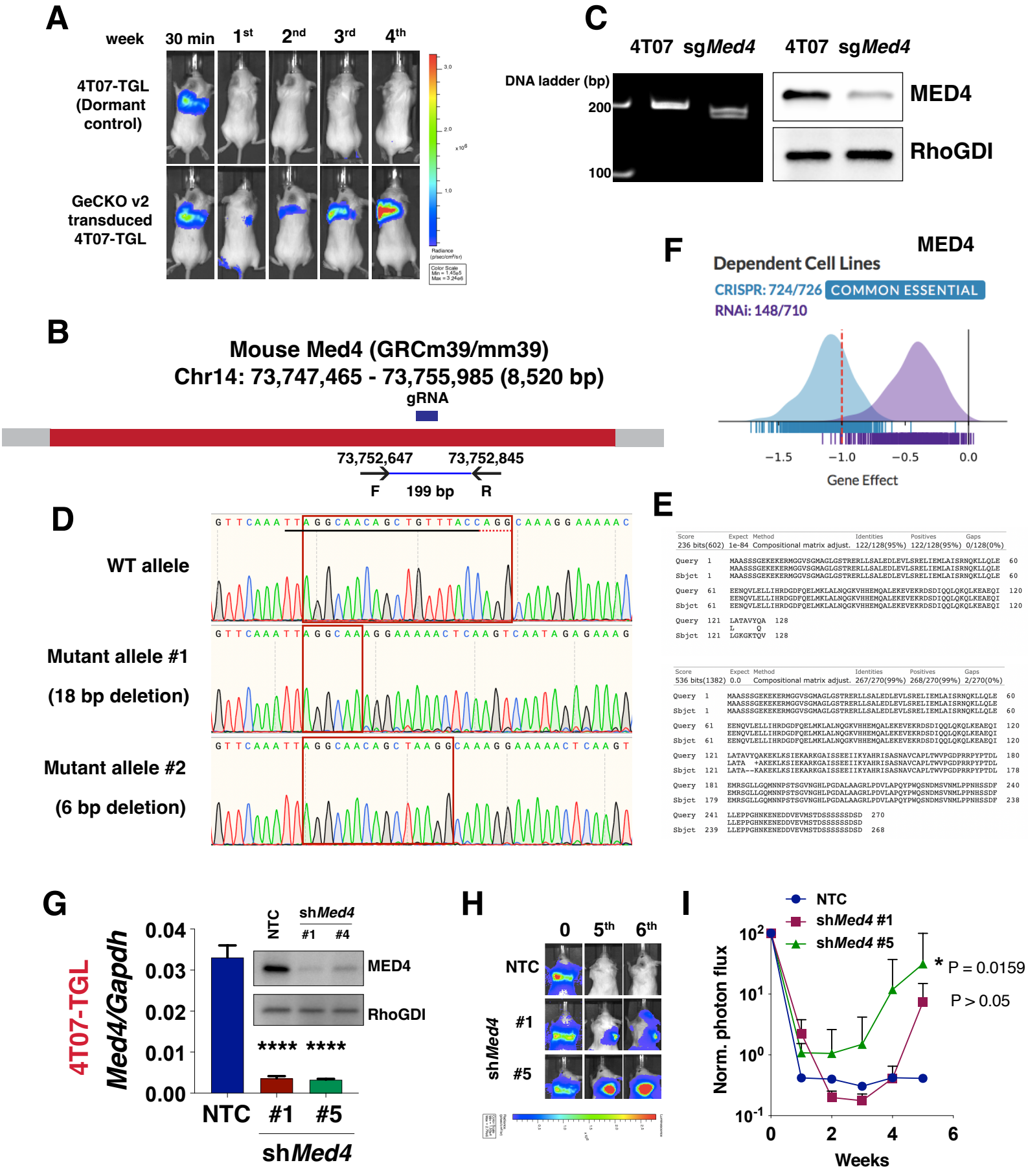

Figure S2 Bae et al.

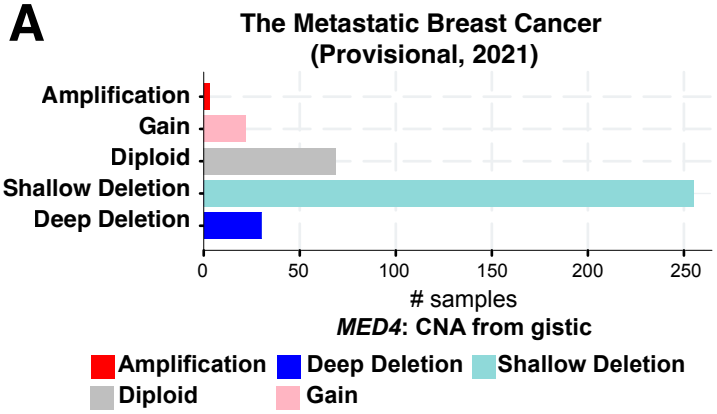

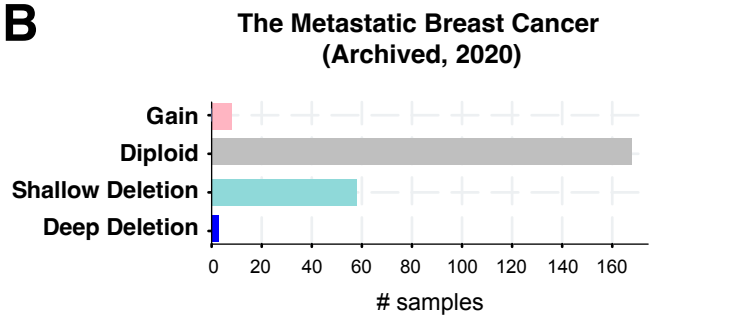

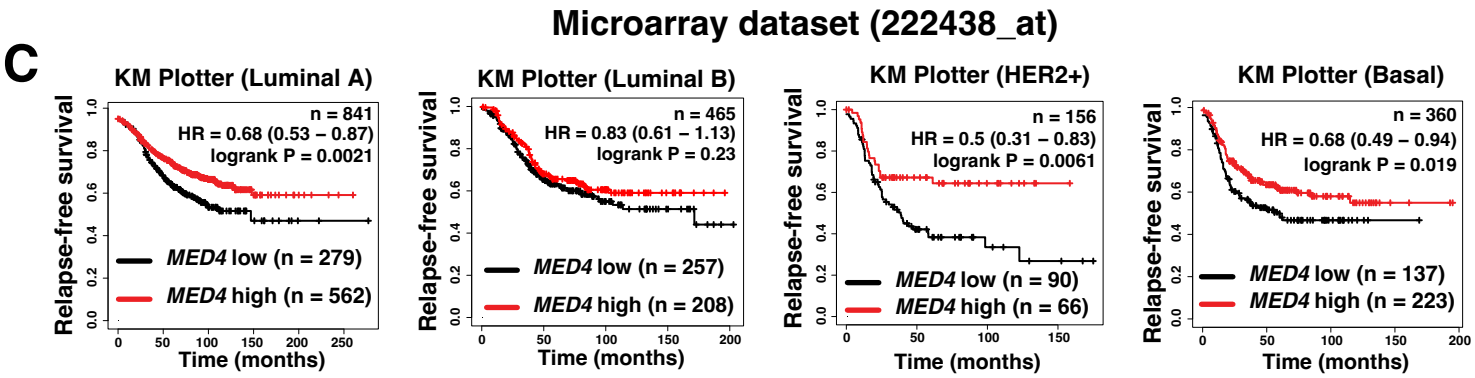

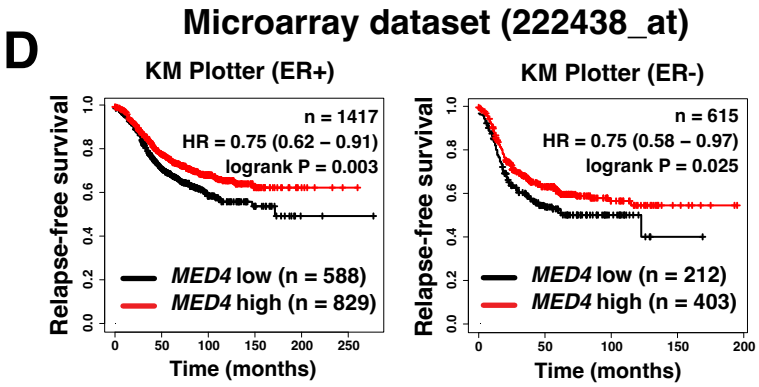

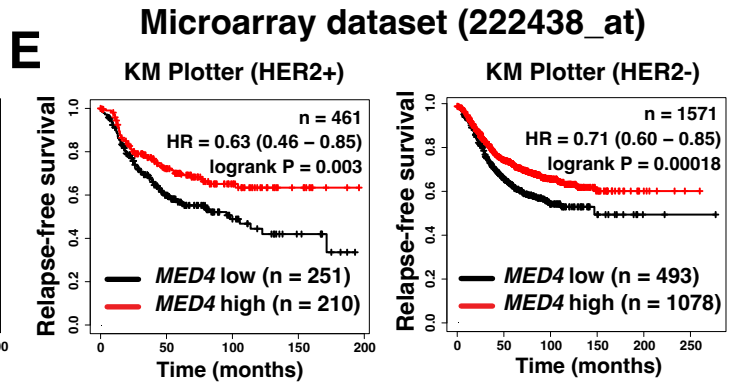

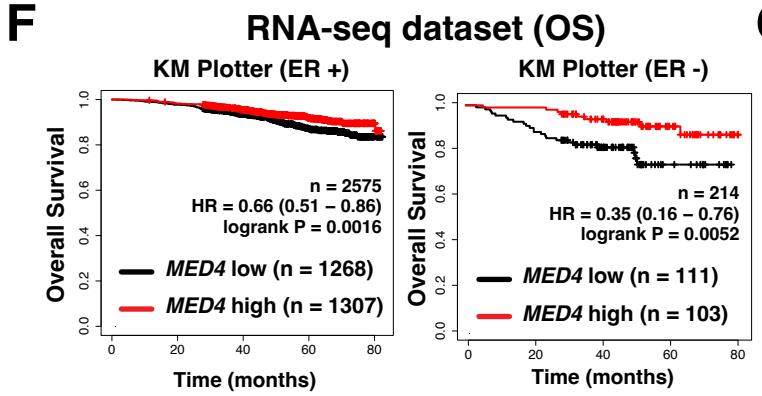

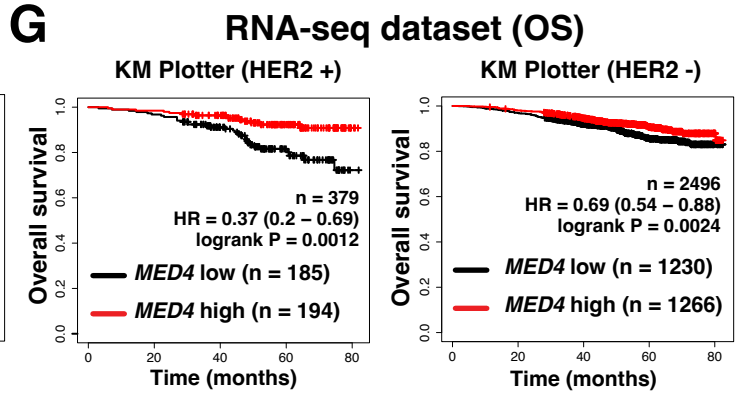

Figure S3 Bae et al.

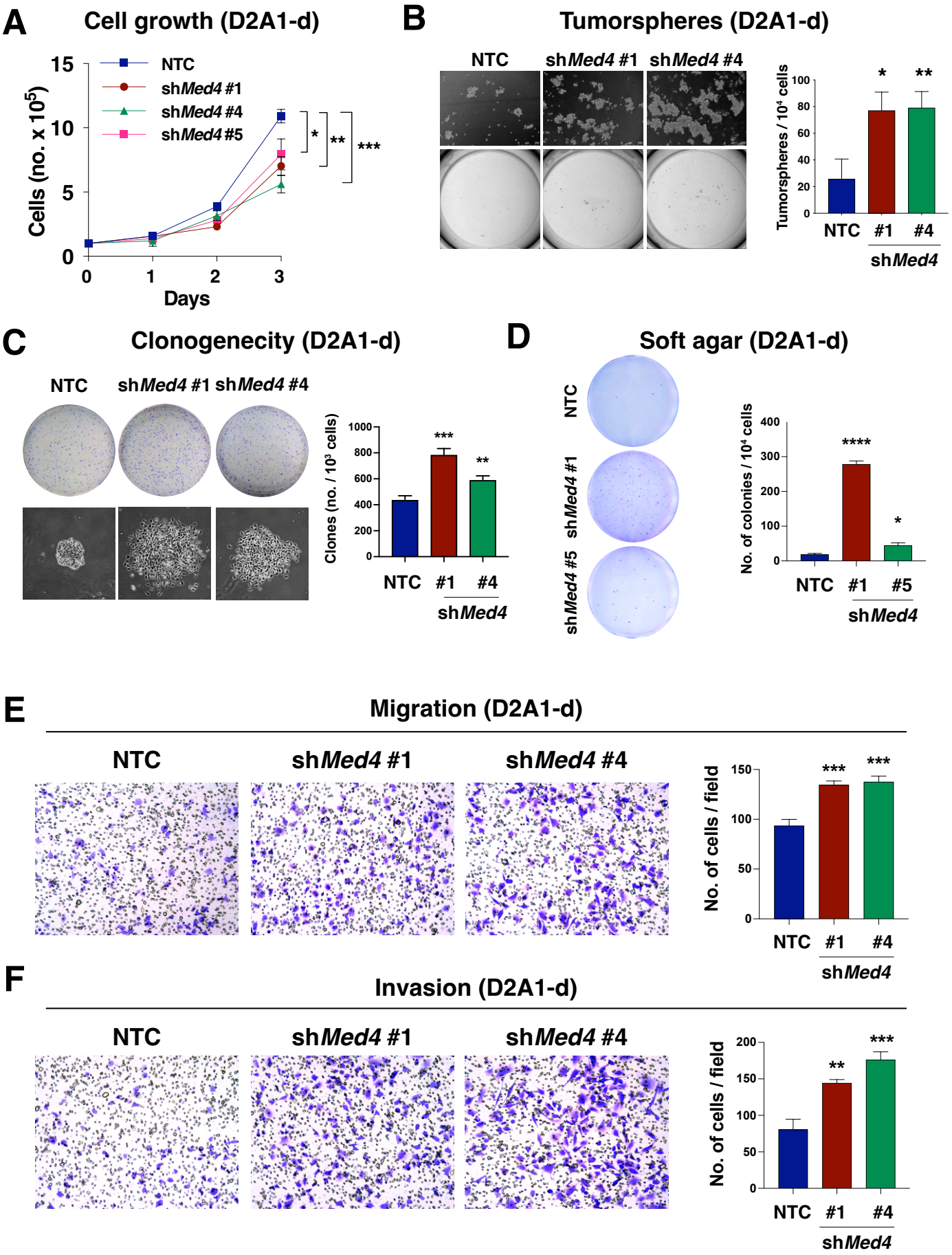

Figure S4 Bae et al.

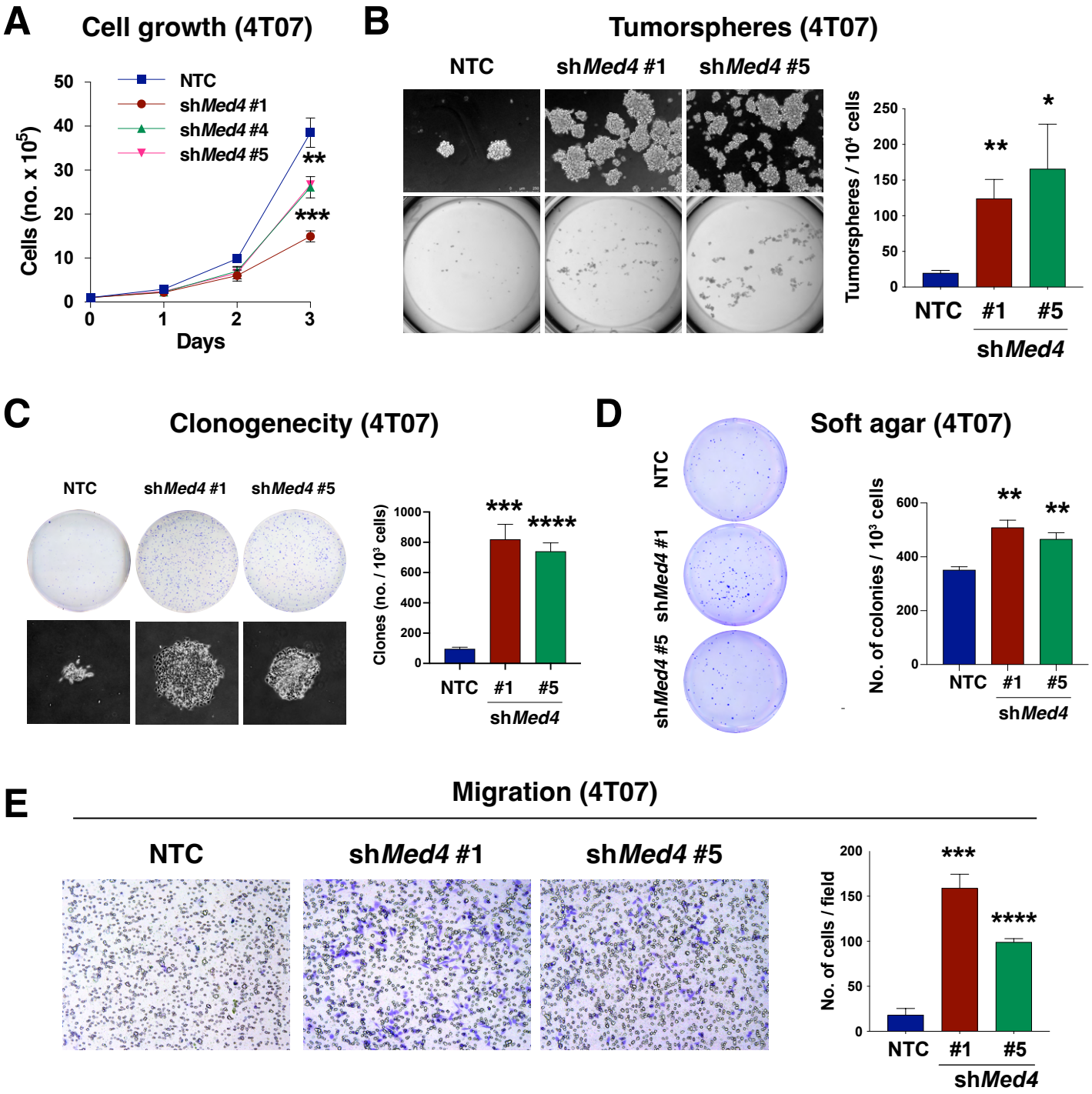

Figure S5 Bae et al.

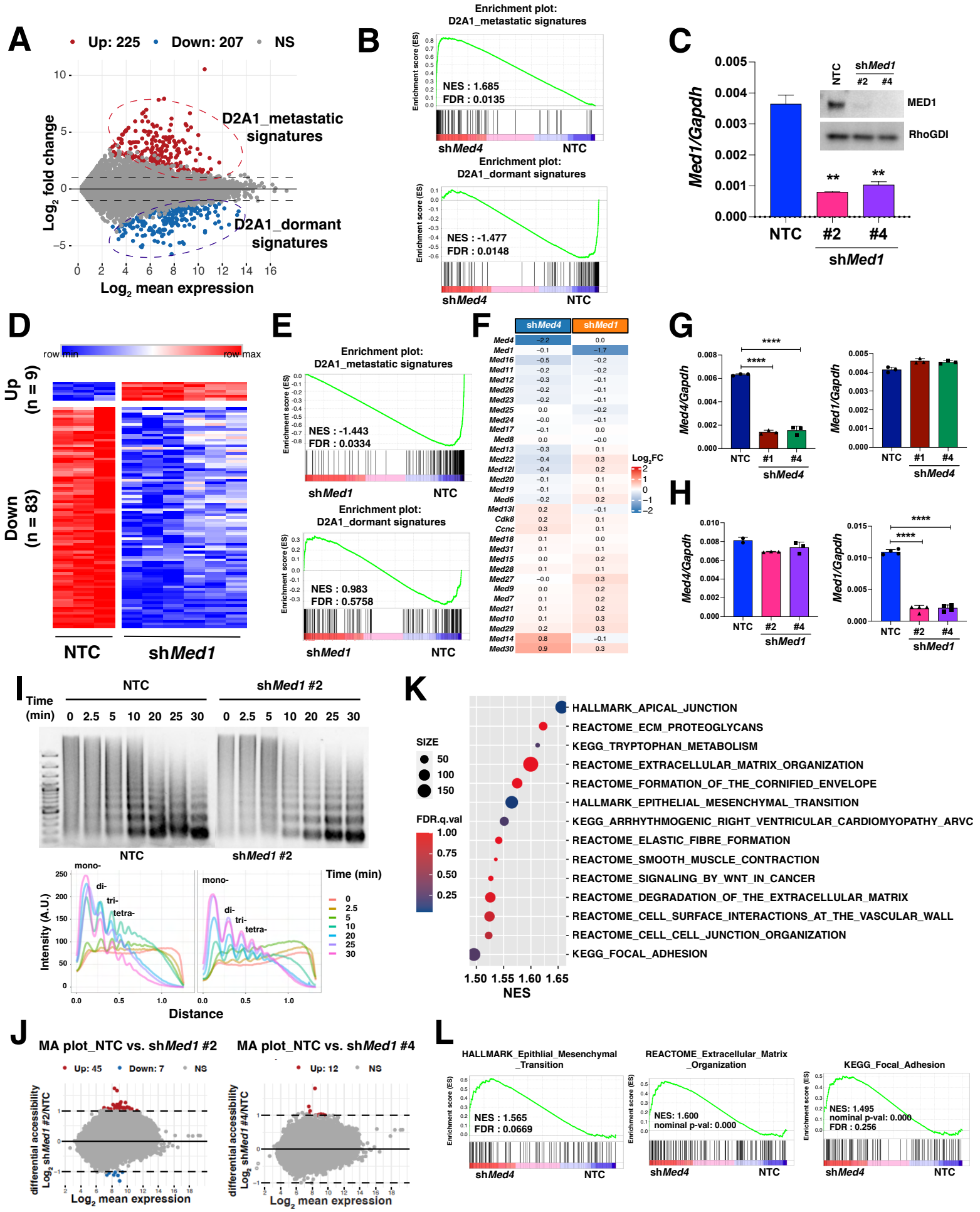

Figure S6 Bae et al.

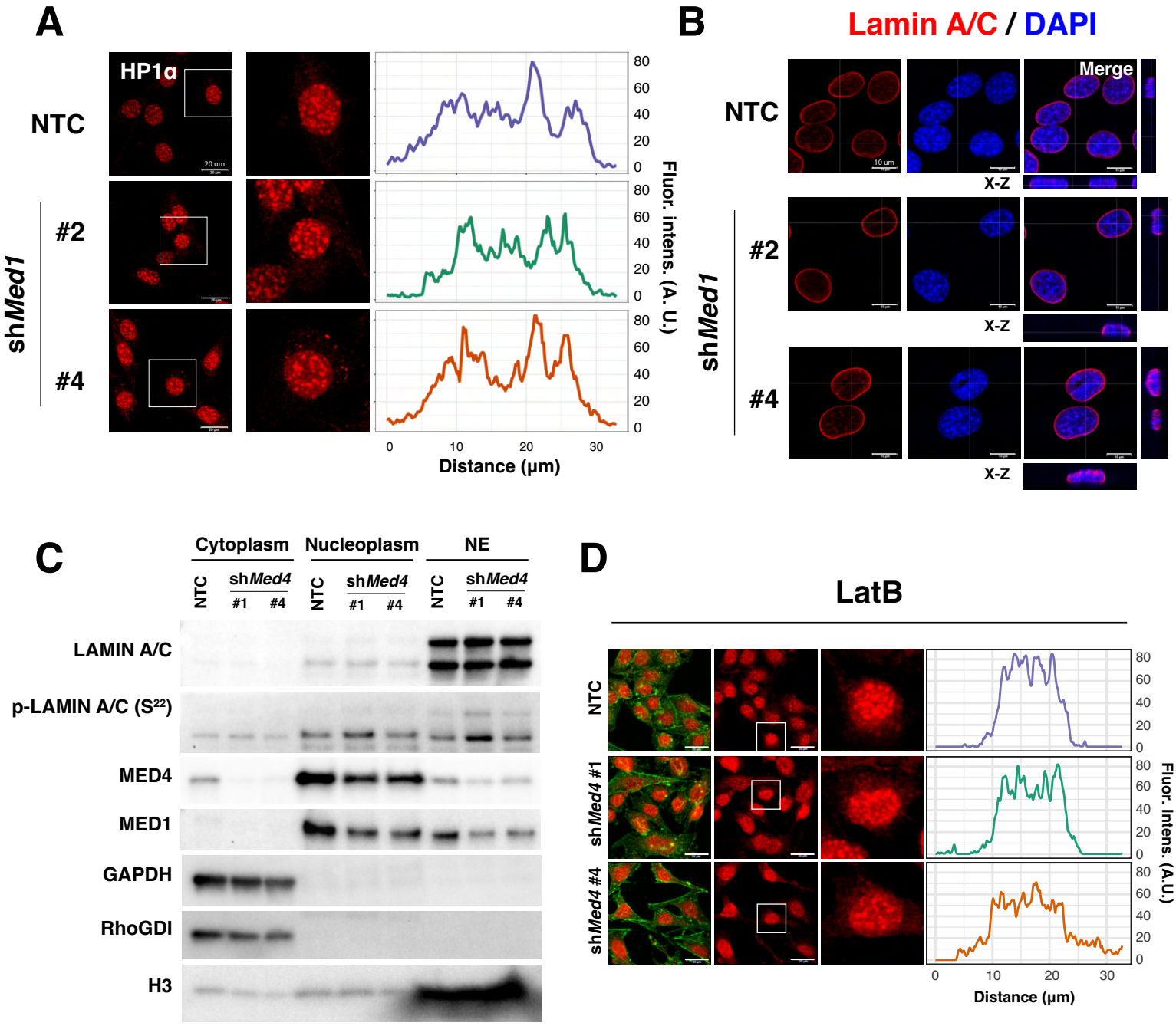
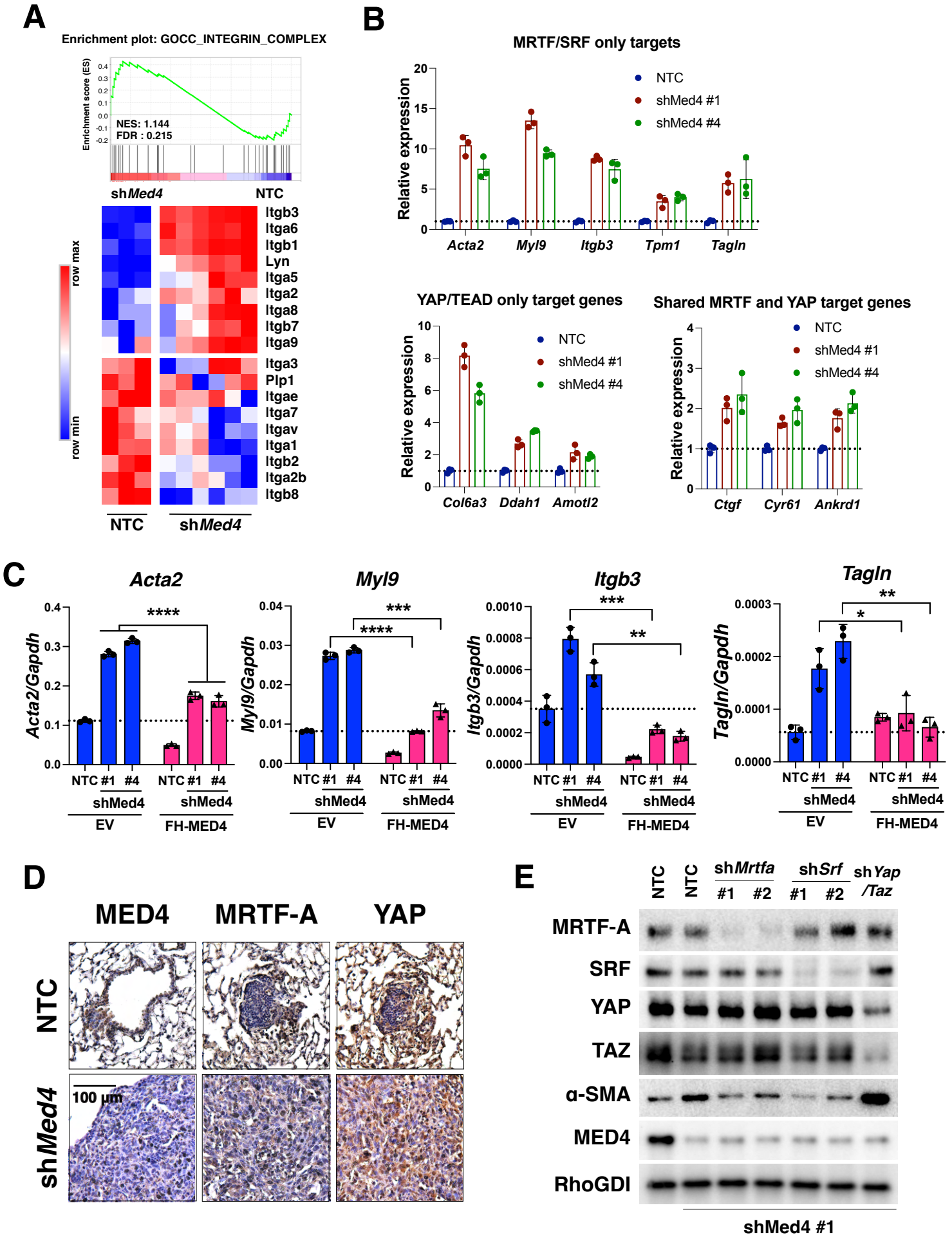
Figure S7 Bae et al.